



저작자표시-비영리-변경금지 2.0 대한민국

이용자는 아래의 조건을 따르는 경우에 한하여 자유롭게

- 이 저작물을 복제, 배포, 전송, 전시, 공연 및 방송할 수 있습니다.

다음과 같은 조건을 따라야 합니다:



저작자표시. 귀하는 원저작자를 표시하여야 합니다.



비영리. 귀하는 이 저작물을 영리 목적으로 이용할 수 없습니다.



변경금지. 귀하는 이 저작물을 개작, 변형 또는 가공할 수 없습니다.

- 귀하는, 이 저작물의 재이용이나 배포의 경우, 이 저작물에 적용된 이용허락조건을 명확하게 나타내어야 합니다.
- 저작권자로부터 별도의 허가를 받으면 이러한 조건들은 적용되지 않습니다.

저작권법에 따른 이용자의 권리는 위의 내용에 의하여 영향을 받지 않습니다.

이것은 [이용허락규약\(Legal Code\)](#)을 이해하기 쉽게 요약한 것입니다.

[Disclaimer](#)

이학박사 학위논문

**Preclinical study of human mesenchymal stem cell  
therapy for bladder dysfunction disorders through  
developing the related animal models and bioimaging  
based monitoring assays**

방광기능장애 동물모델 구축 및  
바이오이미징을 활용한 줄기세포 치료  
전임상 연구

울산대학교대학원  
의학과  
유환열

방광기능장애 동물모델 구축 및  
바이오이미징을 활용한 줄기세포 치료  
전임상 연구

지도교수      주명수  
지도교수      신동명

이 논문을 이학박사 학위논문으로 제출함

2018년 12월

울산대학교대학원  
의학과  
유환열

유환열의 이학박사 학위논문을 인준함

위원장	박	형	근	(인)
부위원장	오	승	준	(인)
부위원장	송	상	훈	(인)
부위원장	신	동	명	(인)
위원	주	명	수	(인)

울산대학교대학원

2018년 12월

**A thesis of the Doctor's degree**

**Preclinical study of human mesenchymal stem cell  
therapy for bladder dysfunction disorders through  
developing the related animal models and bioimaging  
based monitoring assays**

**The Department of Biomedical Sciences**

**University of Ulsan**

**College of Medicine**

**HwanYeul Yu**

**Preclinical study of human mesenchymal stem cell  
therapy for bladder dysfunction disorders through  
developing the related animal models and bioimaging  
based monitoring assays**

**Thesis Director : Myung-soo choo**

**Dong-Myung Shin**

**A thesis submitted to the Department of Biomedical  
Sciences in partial fulfillment of the requirements for the  
Degree of Doctor of Philosophy in Medical Science  
at University of Ulsan College of Medicine**

**December 2018**

**The Department of Biomedical Sciences**

**University of Ulsan**

**College of Medicine**

**HwanYeul Yu**

## ABSTRACT

### **Chapter 1. Improved efficacy and in vivo cellular properties of human embryonic stem cell derivative in a preclinical model of bladder pain syndrome.**

Interstitial cystitis/bladder pain syndrome (IC/BPS) is an intractable disease with pelvic pain and frequent urination. IC/BPS has characteristic cystoscopy findings such as Hunner's ulcer. Also, it is characterized by severe bladder inflammation reaction and urothelium denudation. A promising approach to treat such IC/BPS is with mesenchymal stem cell (MSC) therapy. Currently, adult bone marrow (BM) therapy is known as a method for treating IC/BPS, but there is a limitation of treatment. The effects of pluripotent stem cells (M-MSCs) derived from human embryonic stem cells (hESCs) were demonstrated by transplanting the characteristics of M-MSCs into living animals. Pure M-MSC showed characteristics of typical M-MSC behavior through controlled hESCs differentiation and isolation process. Induction hydrochloric IC/BPS animal model in infusion, bladder, mast cell infiltration, tissue fibrosis, apoptosis start urothelial exposure include functional and histological IC/bladder of BPS and built with superior efficacy compared to improve BM-MSC for improving urination of damage Irritability. Side effects such as abnormal proliferation, tumor formation, or immune-mediated transplant rejection have been observed over 12 months after injection. *In vivo*, confocal microscopy images have confirmed the persistence of cells transplanted in living animals for more than 6 months. The injected M-MSCs are differentiated into different types of cells and gradually become a blood vessel-like structure. In this study, the treatment effect, long-term stability, biodistribution and cellular properties of hESC derivative in pre-clinical models of IC/BPS has demonstrated the improved effectiveness.

**Keywords:** Interstitial cystitis/bladder pain syndrome; Multipotent stem cells; Human embryonic stem cells; Living animal confocal imaging.

## **Chapter 2. Development of reliable chronic bladder ischemia rat model for reproducing the detrusor underactivity**

**Purpose:** To establish a reliable detrusor underactivity (DUA) rat model and to investigate the pathophysiology of chronic bladder ischemia (CBI) on voiding behavior and bladder function.

**Methods:** Adult male rats were divided into five groups. The arterial injury (AI) group underwent vascular endothelial damage (VED) of the iliac arteries (AI-10, 10 times of injury at each iliac artery; AI-20, 20 times; AI-30, 30 times) and received a 2% cholesterol diet. The sham group underwent sham operation and received a 2% cholesterol diet. The control group received a regular diet. After 8 weeks, all rats underwent 24-hour voiding pattern analysis and unanesthetized cystometrogram. Thereafter, bladder tissues and iliac arteries were processed for organ bath investigation, immunohistochemistry staining, and gene expression analysis.

**Results:** The 24-hour voiding pattern analysis showed that in the AI-30 group, micturition interval was significantly increased ( $p < 0.001$ ), and number of voiding and voiding volume were significantly decreased ( $p < 0.01$  and  $p < 0.001$ ). Cystometrogram showed that the frequency of voiding contractions and micturition pressure were significantly lower in the AI-30 group ( $p < 0.01$ ). In the organ bath study, contractile responses to various stimuli were significantly lower in AI-20 and AI-30 group (all  $p < 0.001$ ). Histological study showed that in the AI-20 and AI-30 group atherosclerotic occlusion in the iliac arteries, followed by tissue inflammation, fibrosis, denervation, and apoptosis of the bladder muscle tissue were prominently observed than in sham group. Genome-wide gene expression analysis revealed that genes related to IL-17 and HIF-1 signaling pathways including INF- $\gamma$

receptor-1 and Cxcl2 were up-regulated in the CBI-induced DUA rat model.

**Conclusions:** A rat model of progressive VED without any of artificial enhancers successfully induced the DUA, depending on severity of ischemia injury. Oxidative stress from progressive VED followed by tissue inflammation, fibrosis, denervation, and apoptosis of the bladder muscle tissue can be the possible explanation for the CBI-induced DUA.

**KEY WORDS:** Animal model; detrusor underactivity; Arterial Injury; Chronic Bladder Ischemia

# CONTENTS

Abstract in English .....	i
Contents .....	v
List of Figures .....	vi
List of Abbreviations .....	viii
Chapter 1 .....	1
Improved efficacy and in vivo cellular properties of human embryonic stem cell derivative in a preclinical model of bladder pain syndrome.	
Introduction .....	2
Materials and Methods .....	4
Results .....	10
Discussion .....	42
Chapter 2 .....	46
Development of reliable chronic bladder ischemia rat model for reproducing the detrusor underactivity.	
Introduction .....	47
Materials and Methods .....	49
Results .....	53
Discussion .....	67
Reference .....	72
Abstract in Korean .....	80

## LIST OF FIGURES

### Chapter 1

<b>Figure 1-1.</b> Isolation and characterization of hESC-derived M-MSCs. ....	11
<b>Figure 1-2.</b> M-MSC injection restored bladder function in HCl-IC model rats. ....	15
<b>Figure 1-3.</b> Histological analysis of M-MSC injection effects on HCl-induced bladder injury. .....	17
<b>Figure 1-4.</b> The effect of M-MSC injection on visceral hypersensitivity in HCl-IC model rats. .....	20
<b>Figure 1-5.</b> Central role of Wnt and IGF signaling activity on therapeutic effect of M-MSCs. .....	23
<b>Figure 1-6.</b> Immunostaining of b-catenin in the bladder after M-MSC therapy. ....	25
<b>Figure 1-7.</b> Effect of Wnt or IGF signaling inhibition on M-MSCs therapy for treating HCl- induced IC. ....	26
<b>Figure 1-8.</b> Immunostaining analysis for cellular properties of transplanted M-MSCs. ...	29
<b>Figure 1-9.</b> Longitudinal confocal imaging of transplanted M-MSCs in living animals. ...	31
<b>Figure 1-10.</b> Intravital confocal imaging of the transplanted M-MSCs. ....	33
<b>Figure 1-11.</b> Superior therapeutic efficacy of M-MSCs compared to BM-MSCs. ....	37
<b>Figure 1-12.</b> Bioluminescence assay of transplanted M-MSCs. ....	39
<b>Figure 1-13.</b> Limitation of BM-MSCs about in vivo engraftment. ....	40
<b>Figure 1-14.</b> micro-PET/MRI imaging assay of transplanted M-MSCs. ....	41

## **Chapter 2**

<b>Figure 2-1.</b> CBI modeling schematic diagram and voiding diary for 24hours. ....	54
<b>Figure 2-2.</b> Cystometrogram analysis. ....	56
<b>Figure 2-3.</b> Assessment of bladder smooth muscle contraction. ....	58
<b>Figure 2-4.</b> Histologic examination. ....	60
<b>Figure 2-5.</b> Immunofluorescent analysis. ....	63
<b>Figure 2-6.</b> Gene analysis .....	66

## **LIST OF ABBREVIATIONS**

IC/BPS: Interstitial cystitis/bladder pain syndrome

MSCs: Mesenchymal stem cells

M-MSCs: Human embryonic stem cell-derived multipotent stem cells

BM: Bone-marrow

UCB: umbilical cord-blood

SC: stem cell

HCl: hydrochloric-acid

PSC: pluripotent stem cell

ESCs: embryonic stem cells

OP9: supporting feeder cells

IVP: intravesical pressure

IAP: intra-abdominal pressure

NVC: non-voiding contraction

BP: bladder basal pressure

MP: micturition pressure

MV: micturition volume

RV: residual volume

BC: bladder capacity

MI: micturition interval

DUA: detrusor underactivity

CIC: clean intermittent catheterization

LUTS: lower urinary tract symptoms

DO: detrusor overactivity

CBI: chronic bladder ischemia

VED: vascular endothelial damage

AI: arterial injury

L-NAME: nitric oxide synthase inhibitor

# **CHAPTER 1**

**Improved efficacy and in vivo cellular properties of  
human embryonic stem cell derivative in a  
preclinical model of bladder pain syndrome.**

## INTRODUCTION

Interstitial cystitis/bladder pain syndrome (IC/BPS) shows urinary epithelium exfoliation, mast cell activation and sensory nerve hyperactivity, and chronic inflammation of submucosal layer and muscle layer of bladder<sup>1, 2</sup>. Many IC/BPS patients suffer from decreased quality of life due to frequent urination, urgency and sexual dysfunction, sleep disturbance, depression, anxiety and chronic stress, as well as pelvic pain, which can be exacerbated by bladder filling<sup>3, 4</sup>. Prevalence of 0.1% was considered relatively rare, but recent evidence suggests that IC/BPS may be present within > 2% of females<sup>5</sup>. Multiprocessing strategies include IC/BPS including pentosan polysulfate<sup>6,7</sup>, oral formulations, histamine type I receptor antagonists<sup>8</sup>, immune agents<sup>9</sup>, monoclonal antibodies against nerve growth factor<sup>10</sup>, and Hunner lesions<sup>11</sup>, bladder and urethral resection/clotting hydrodistension, but the results are still not often satisfied with the recurrence of symptoms and Hunner lesions<sup>12</sup>. Thus, treatment of IC/BPS remains a clinical challenge and further research on the mechanism of disease onset is needed to identify treatment therapies.

Recently, study reported the beneficial results of mesenchymal stem cells derived from human umbilical cord-blood (UCB) to treat IC/BPS and ketamine-induced cystitis in an *in vivo* rat model<sup>13, 14</sup>. Preclinical and clinical trial data suggest that MSCs are a practical and safe source of cells for SC-based therapies<sup>15-19</sup>. However, in order to treat patients with serious diseases, there is a problem that an alternative cell source is needed to obtain a sufficient cell number of sufficient systematic potential. More importantly, direct assessment of the biological and molecular properties of engrafted cells in the pathological environment has not been performed for current MSC therapies; thus, underlying therapeutic mechanisms, tumorigenic risk after transplantation, and the optimal transplantation protocol are all unclear. More importantly, current MSC therapies do not directly assess the biological and molecular characteristics of transplanted cells in pathological environments. Therefore, with the

underlying treatment mechanism, the risk of post-transplantation tumorigenesis and the optimal transplantation protocol have not been clarified to date. Embryonic SCs (ESCs) are embryonic stem cell embryos that are capable of differentiating into all cell types in the human body, and are capable of expanding into the immortalized cell line *in vitro*<sup>20, 21</sup>. Based on this versatility and infinite scalability, ESCs are considered a promising resource for regenerative medicine<sup>22</sup>. MSC-like cells were recently obtained from human ESCs (hESCs) through epithelial mesenchymal transition; In addition to the porous membrane mediated separation of MSCs, by spontaneous or controlled differentiation with growth factor cocktail and support feeder cells (OP9)<sup>23, 24</sup>. The hESCs have significant advantages, including the ability to generate untreated control cell differentiation control untreated to identify optimal safety and efficacy prior to transplantation, so that the derived mesenchymal stem cells can overcome the disadvantages of current MSC therapy. However, safety issues based on the treatment of hESC will still need to be addressed, including the risk of malformations and other species capable of forming tumors, differentiation as a potential immune responses and unwanted cell types do. In this study, demonstrated recovery of hESCs are derived from multipotent stem cells (M-MSCs) to more effectively improve the pathological characteristics of the functions of urination and the IC/BPS than adult bone marrow, bladder (BM) is the cells induced in animal models IC/BPS is induced by instillation of hydrochloric acid (HCl). In addition, the results of 12 months abnormal growth, tumors, or immune-mediated graft rejection was not observed. More importantly, monitored the *in vivo* distribution and phenotypic characteristics of M-MSCs injected by confocal microscopy and micro-endoscopy in living animals for 6 months after transplantation in the longitudinal direction. This study provides the first evidence for the therapeutic efficacy and long term safety of my biometric characteristics of the offspring of transplanted hESC survival and for IC/BPS therapy.

## MATERIALS AND METHODS

### *Study Approval*

All animal studies in the paper were approved and carried out in accordance with the guidelines and regulations set out in the Ulsan Medical Animal Care and Use Committee (IACUC-2014-14-167).

### *Chapter 1. Study Design*

The aim of the study was to determine the therapeutic efficacy of human ESC-derived MSCs (M-MSCs) superior to BM-based controls to treat IC/BPS in animal models, as well as to longitudinally monitor transplanted *in vivo* cellular properties. *In vitro*, M-MSCs characterize morphological and karyotypic analyzes, versatility, angiogenic efficacy and surface markers and expression of stem cell genes to characterize. *In vivo*, M-MSCs are administered to rat-damaged bladder and evaluated for bladder drainage function, urinary tract infection, mast cell infiltration, histopathology, apoptosis, and tumorigenesis. Observe M-MSC injected for 6 months after transplantation using *in vivo* confocal fluorescence imaging in live animals. For all experimental conditions, two independent sets with 5 independent animals per group were performed. They were randomly assigned to the treatment group, order of injury, order of cell transplantation or vehicle injection, and order of bladder metering. Information on the type and dose of injected cells was masked by the experimenter involved in the surgical procedure. All cystoscopy, histology, and gene expression assessments were performed by blinded investigators in the treatment group. Animals that died unexpectedly due to bladder injury or catheter insertion were excluded from the analysis.

### ***Differentiation and culture of hESC-derived M-MSCs and human BM-derived MSCs***

Retention of undifferentiated H9-hESC and differentiation into M-MSC (**Fig. 1-1a**) was performed as previously described<sup>23, 24</sup>. The established M-MSCs were suspended in EGM2-MV medium (Lonza, San Diego, CA, USA) on plates coated with rat tail collagen type I (Sigma-Aldrich, St. Louis, Mo., USA) in a humidified atmosphere with 5% CO<sub>2</sub> at 37°C. All M-MSCs used in the experiments were extended to less than 10 passages to ensure differentiation. Specificity of basic features such as surface protein expression, cell proliferation, pluripotency (osteogenesis, cartilage formation or *in vitro* differentiation into adipocytic lineage), *in vitro* angiogenesis analysis and karyotyping was performed as previously described<sup>23, 24</sup>. The M-MSC system stably expressing GFP was established by infection with the GFP-expressing lentivirus produced as described above<sup>13</sup>. Human BM-MSCs purchased from Lonza (Basel, Switzerland) were cultured according to the manufacturer's instructions. The cells expanded to less than 7-passage in the experiment to ensure multiplicity. All cells were examined monthly for mycoplasma content (Mycoplasma Hoechst Stain Kit; 3030000, MP Biomedicals, LLC, Santa Ana, CA, USA).

### ***Animal models and transplantation of M-MSCs***

The HCl injected IC/BPS rat model was established as previously described<sup>13</sup>. 1-week after the HCl injury, a low abdominal incision was made and the indicated amount of hESC-derived M-MSCs or PBS vehicle was injected directly into the outer layer of the dorsal wall and dome of the bladder using a 500 µm syringe and a 26-gauge needle as reported previously<sup>13, 14, 54</sup>. Starting from 1 day prior to stem cell injection, indomethacin (PMG Pharm Co., Ltd. Ansan, Korea; every 12 h at 2.5 mg/kg) or Gefitinib (Santa Cruz Biotechnology, Santa Cruz, CA, USA; every day at 5 mg/kg) were subcutaneously injected to block Wnt or IGF mediated signals.

***Unanesthetized and unrestrained cystometrogram acquisition (awake cystometry)***

Cystoscopy was performed on unanesthetized and unrestrained rats in the cage with the metabolic cages. Simultaneous catheterizations for intravesical pressure (IVP) and intra-abdominal pressure (IAP) recordings were performed 3 days prior to before the bladder pressure test as described previously<sup>55, 56</sup>.

Briefly, after induction of anesthesia, a caged polyethylene container (PE-50, Becton-Dickinson, Parsippany, NJ, USA) was implanted in the dome of the bladder via an abdominal incision. An abdominal balloon (Latex, Daewoo Medical, Incheon, Korea) around the cuff of the catheter tip was placed in the bladder proximal to connect with the other catheter using a silk seal to record the IAP. The polyethylene catheter (PE-50) was heated with warm water, stretched 1.5 times in length at the end of the insertion face, and filled with heparinized saline (100 IU/mL). After implanting the bladder catheter, an extended catheter was inserted into the femoral vein. The catheter passes through the tunnel through the subcutaneous space, and then exits to the back of the animal and is fixed to the skin on the back. After surgery, each rat was individually housed and maintained in the same manner. To awake cystometric analysis, the catheter catheter into the bladder was inserted through a T-tube into a 2-way valve and a microinjection pump (PHD22/2000 pump) connected to a pressure transducer (Research Grade Blood Pressure Transducer, Harvard Apparatus, Holliston, MA, USA), Harvard Apparatus). IAP was recorded by connecting another intrinsic catheter connected to a fluid-filled abdominal balloon to another pressure transducer. The urine volume was continuously recorded by a fluid collector connected to a Research Grade Isometric Transducer (Harvard Apparatus) while aseptic physiological saline was infused into the bladder at a rate of 0.4 mL/min. IVP, IAP and urine volume were continuously recorded using the MP150 data acquisition system with Acq Knowledge 3.8.1 software (Biopac Systems, Goleta, CA, USA) at a sampling rate of 50 Hz. The values of all reproducible voiding cycles measured for 8 minutes from individual animals were used for

evaluation. Non-voided contractions (NVC) were calculated when the increase in IVP exceeded 15 cm H<sub>2</sub>O from the baseline without voids. BP was defined as the lowest bladder pressure at fullness, the maximum bladder pressure during the voiding cycle, Micturition pressure (MP) was defined as the IAP-maximum bladder pressure. MV was the urine volume of the discharged urine, and RV was the volume of the urine remaining after voiding. BC was defined as MV+RV and MI as drainage contraction interval.

### ***Histological and gene expression analyses***

Epithelial denudation was assessed by immunostaining for cytokeratin, mast-cell infiltration by Toluidine blue staining (8544-4125; Daejung Chemicals & Metals, Seoul, Korea), tissue fibrosis by Masson's trichrome staining (Junsei Chemical, Tokyo, Japan), and apoptosis by TUNEL staining (1 684 795; Roche, Mannheim, Germany) as previously described<sup>14</sup>. Tracking of injected GFP<sup>+</sup> M-MSCs in the bladder was performed by immunofluorescent staining with a specific rabbit GFP polyclonal antibody (ab290; Abcam, Cambridge, MA, USA). Epithelial cells, stromal cells and endothelial cells of GFP<sup>+</sup> cells were characterized by E-cadherin (612130; Clone 36; FITC-conjugated, BD Biosciences, San Diego, CA, USA), vimentin (sc-6260; Santa Cruz Biotechnology), CD31 (sc-376764, Santa Cruz Biotechnology). Wnt activation was examined by immunofluorescent staining of  $\beta$ -catenin (sc-7199; Santa Cruz Biotechnology). Immunostaining was visualized using Alexa 488 (A11001) or 564 (A11010) conjugated anti-mouse or -rabbit antibody (Molecular Probes, Grand Island, NY, USA). The nuclei were counterstained with 4', 6-diamino-2-phenylindole (D9542; DAPI, Sigma-Aldrich).

### ***Gene expression analyses***

For gene expression analysis, preparation of total RNA was performed using an RNeasy Mini Kit (Qiagen Inc., Valencia, CA), reverse transcription using TaqMan Reverse

Transcription Reagents (Applied Biosystems), and real-time quantitative PCR (RQ-PCR) of the indicated transcripts with the PikoReal Real-Time PCR System (Thermo Scientific) and iQ SYBR Green PCR Master Mix (Bio-Rad, Hercules, CA) as described<sup>57</sup>. Gene expression data was obtained from duplicate RQ-PCR analysis (n = 10) from 5 animals randomly selected per group.

### ***Animal $\mu$ -PET/MRI imaging***

Ten HCl-based IC/BPS rats were randomly divided into two groups and injected with  $1 \times 10^6$  M-MSC (n=5) or PBS vehicle (n=5).  $\mu$ -MRI/PET imaging was performed at 6, 9, and 12 months after injection using a nanoScanPET/MRI imaging system (1T, MEDISO, Budapest Hungary). Rats were fasted for 8 hours before imaging. The rats were heated under anesthesia (2% isoflurane in 100% O<sub>2</sub> gas) to deliver  $19.7 \pm 1.1$  MBq in 0.2 mL of 2-[<sup>18</sup>F]-FDG through the tail vein and warmed using heated air. During the FDG uptake, a T1-weighted gradient-echo (GRE) 3D sequence (TR= 25 ms, TE<sub>eff</sub>= 3, FOV= 64 mm, matrix= 128  $\times$  128) was obtained. Static PET images were acquired over a 15-minute period from 1-5 matches in a single view of the MRI range. Body temperature was maintained by flowing heated air through the animal bed (Multicell, Mediso, Hungary) and the pressure-sensitive pad was used for breathing induction. The PET images were reconstructed using Tera-Tomo 3D in full detector mode with all modifications for high normalization and 8 iterations.

### ***BRET imaging of M-MSCs***

The M-MSCs were infected with a retrovirus containing Nano-lantern structure that was kindly provided by Prof. Takeharu Nagai<sup>34</sup>. BM-MSCs ( $2 \times 10^5$  in 100  $\mu$ l saline) or Labeled M-MSCs were injected into the bladder of mice in which chronic bladder inflammation was induced by intraperitoneal administration of cyclophosphamide (CYP, 100 mg/kg, Sigma-Aldrich) every two days for one week<sup>35</sup>. Bioluminescence imaging was performed using

IVIS Spectrum Pre-clinical *In vivo* Imaging System and Living Imaging 4.4 software (PerkinElmer, Waltham, MA) according to the manufacturer's instructions and previously published protocol<sup>34</sup>.

### ***Longitudinal in vivo confocal imaging using $\mu$ -endoscopy and microscopy***

M-MSCs infected with GFP-expressing lentivirus ( $1 \times 10^6$ ) were directly injected into the bladder of HCl-IC rats and confocal imaging of the M-MSCs injected from live animals using  $\mu$ -endoscopic optical probes or objective lenses for 6 months after transplantation. A small incision (below 5-mm) was made in the upper abdominal skin and the outer surface of the bladder was slightly exposed to all contact with the objective lens. The micro endoscope probe was developed using triplet GRIN lenses configured for front-view imaging<sup>36</sup>. The manufactured endoscope had a diameter of 1.2 mm, a length of 5.5 cm, and lateral and lateral resolutions of 1  $\mu$ m and 11  $\mu$ m, respectively, which were sufficient for single cell analysis. Designed probes were mounted on a custom confocal microscope system and optically aligned to the system using a precise XYZ translational stage. By operating the continuous 488 nm laser excitation, the GFP emission signal was detected and 2D-fluorescent image was acquired at 30 frames/s.

### ***Statistical analysis***

Data were reported as mean  $\pm$  standard error (SEM) of the mean and analyzed with GraphPad Prism 6.0 software (GraphPad Software, La Jolla, Calif.). Treatment group differences were tested for significance by one-way or two-way ANOVA then Bonferroni post hoc test. Statistical significance was defined as #  $p < 0.05$ , ##  $p < 0.01$ , ###  $p < 0.001$ , \*  $p < 0.05$ , \*\*  $p < 0.01$ , \*\*\*  $p < 0.001$ .

## RESULTS

### *Characterization of M-MSCs derived from hESCs*

The hESC line H9 was differentiated for 2 days by embryonic body (EB) formation, and mesenchymal cells were separated and moved to the lower section of a porous transwell membrane (8  $\mu\text{m}$ ) for 5 days (**Fig. 1-1a**). Plating of migrated cells onto collagen-coated plate naturally selected  $\text{CD140B}^+\text{CD44}^+$  M-MSCs thus resulting in over 99% of 23-M pure mesenchymal stem cells in the control hESC differentiation 7 days<sup>24</sup>. The M-MSCs have several typical MSC functions, including spindle and fibroblast-like morphology (**Fig. 1-1b**), expression of MSC (CD73 and CD105) and pericyte (PDGFRB, CD146, and NG2) surface antigens. However, MHC class II (HLA-DR), hematopoietic progenitor (CD133) or endothelial cell (KDR and Tie-2) markers were scarcely expressed (**Fig. 1-1c**). They have the ability to differentiate into mesodermal bone formation and adipocyte lineage (Fig. 1-1e) and substantially downregulated markers of pluripotency (OCT4, NANOG, and SOX2), and upregulated expression of EMT markers such as fibronectin, consistent with MSC-like characteristics.<sup>24</sup> Established mesenchymal stem cells can be expanded to more than 30 passages (once a day) without changes in chromosomes (**Fig. 1-1d**). In addition, M-MSCs exhibited tube-forming capacity on Matrigel (**Fig. 1e**) and also formed functional junctions with blood vessel endothelial cells, as evidenced by dye transfer assay (**Fig. 1f**), indicating robust pro-angiogenic potency.

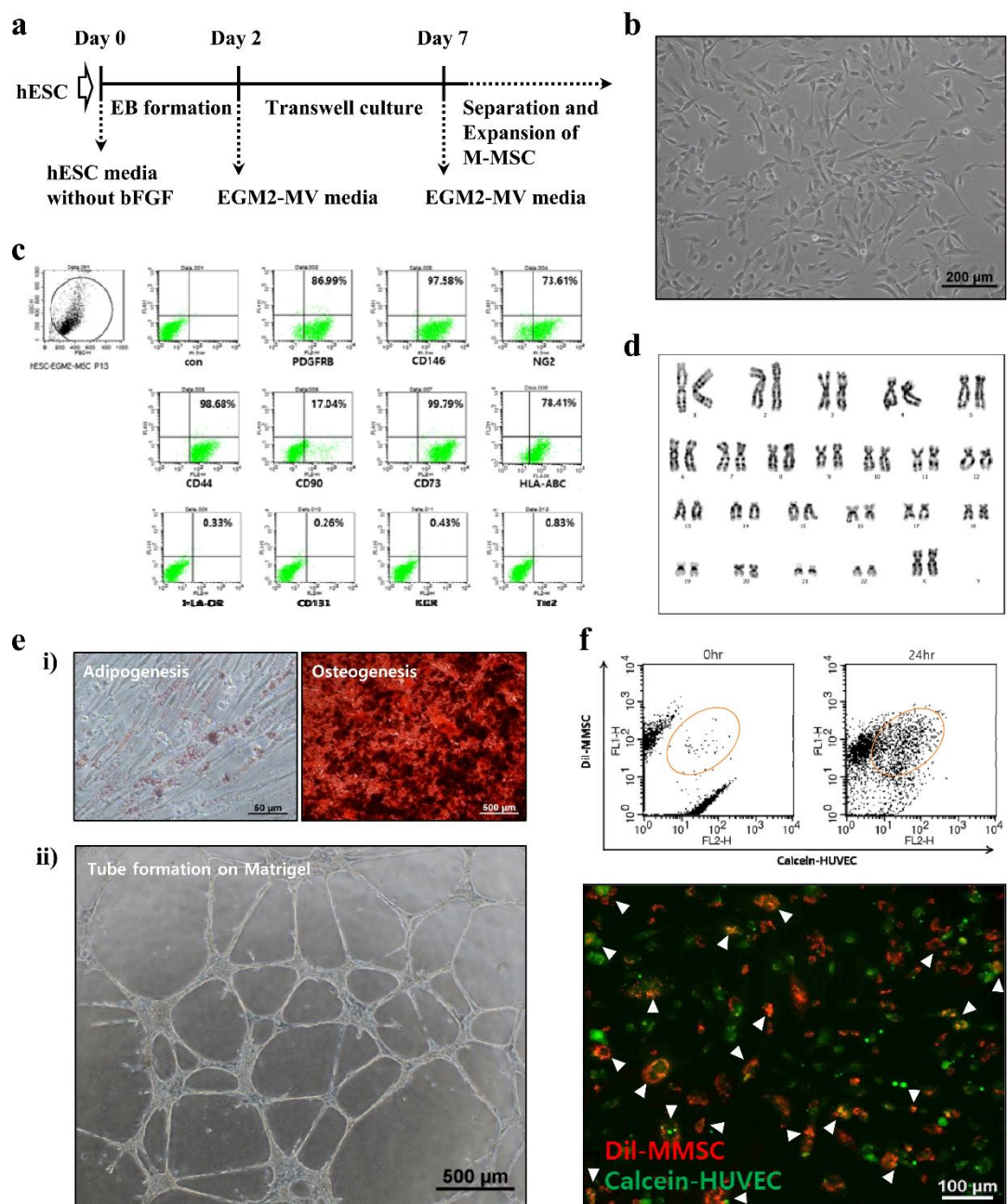


**Figure 1-1. Isolation and characterization of hESC-derived M-MSCs.**

(a) Experimental scheme for the transwell-based differentiation. (b) Morphological characterization of M-MSCs. Scale bar = 200 μm. (c) M-MSCs at passage of 8 were analyzed for specific surface antigen marker expression for hMSCs (CD44, CD90, and CD73), pericytes (PDGFRB, CD146, and NG2), endothelial cells (KDR and Tie-2),

hematopoietic progenitors (CD133), and MHC class I (HLA-ABC) and II (HLA-DR). **(d)** Karyotypic analysis of M-MSCs at passage 19. The isolated cells were capable of stable proliferation without chromosomal changes. **(e)** i) Differentiation potential of M-MSCs was shown by adipogenesis (left, Oil red staining, scale bar = 50  $\mu$ m) and osteogenesis (right, Alizarin red staining, scale bar = 500  $\mu$ m). ii) *In vitro* tube assembly assay. Scale bar = 500  $\mu$ m. **(f)** Dye transfer (circle in the plot) increased in a coculture of DiI-labeled M-MSCs (M-MSC-DiI, red) and calcein-labeled human umbilical vein endothelial cells (HUVEC-Calcein, green). Dye-transfer between M-MSCs and HUVECs was visualized by fluorescence microscopy (white arrowheads).

### ***In vivo therapeutic potency of M-MSC for treating IC/BPS***

The IC/BPS animal model established by HCl injection was used to examine the *in vivo* efficacy of M-MSC<sup>13</sup>. Analysis of the bladder function using awake cystometry showed irregular voiding and decreased micturition intervals (MI) in IC/BPS rats (HCl-IC group) in which HCl injection was induced compared to sham-operated (sham) rats (23.93±2.19 s vs. 108.7±4.53 s; p<0.001), in addition, low urine volume (MV; 0.090±0.010 vs. 0.395±0.022 mL; p<0.001), micturition pressure (MP; 19.36±1.63 vs. 56.24±4.62 cm H<sub>2</sub>O; p<0.001), bladder capacity (BC; 0.156±0.014 vs. 0.691±0.030 mL; p<0.001), and residual volume (RV; 0.121±0.007 vs. 0.329±0.022 mL; p<0.001) (**Fig. 1-2a** and **1-2b**). IC/BPS rats also showed increased maximum pressure (111.90±8.17 vs. 76.12±5.99 cm H<sub>2</sub>O; p<0.01) and bladder basal pressure (BP; 44.83±11.87 vs. 18.58±3.76 cmH<sub>2</sub>O; p<0.05) compared to shams (**Fig. 1-2b**). A single transplantation of 1 x 10<sup>6</sup> M-MSCs (HCl-IC + M-MSC group) significantly improved these defective voiding parameters. This beneficial effect was observed by administration of more than 2.5 x 10<sup>5</sup> M-MSCs (**Fig. 1-2a** and **1-2b**) and was sustained for 2- or 4-weeks after transplantation (**Fig. 1-2c**). In particular, animals of the HCl-IC group typically have increased contraction frequency during the non-void period (NVC) that was significantly improved by M-MSC treatment even at low doses (2.5 x 10<sup>5</sup>) of M-MSCs (**Fig. 1-2b** and **1-2c**).

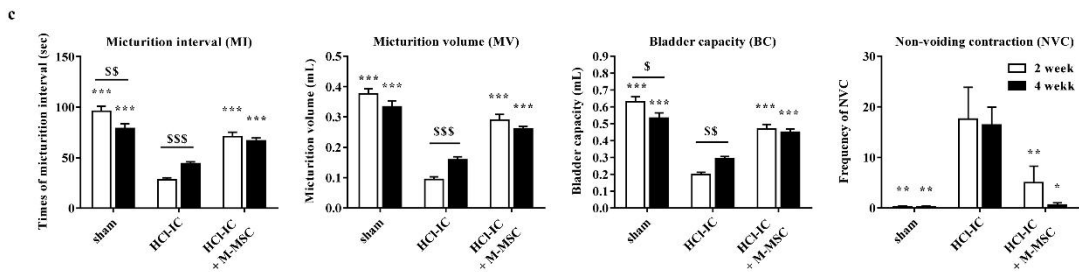
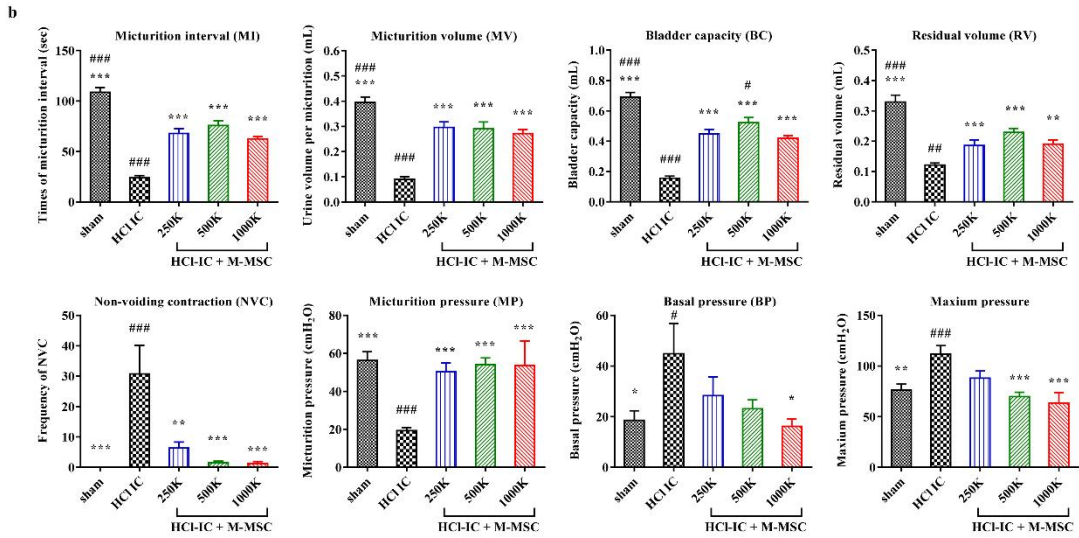
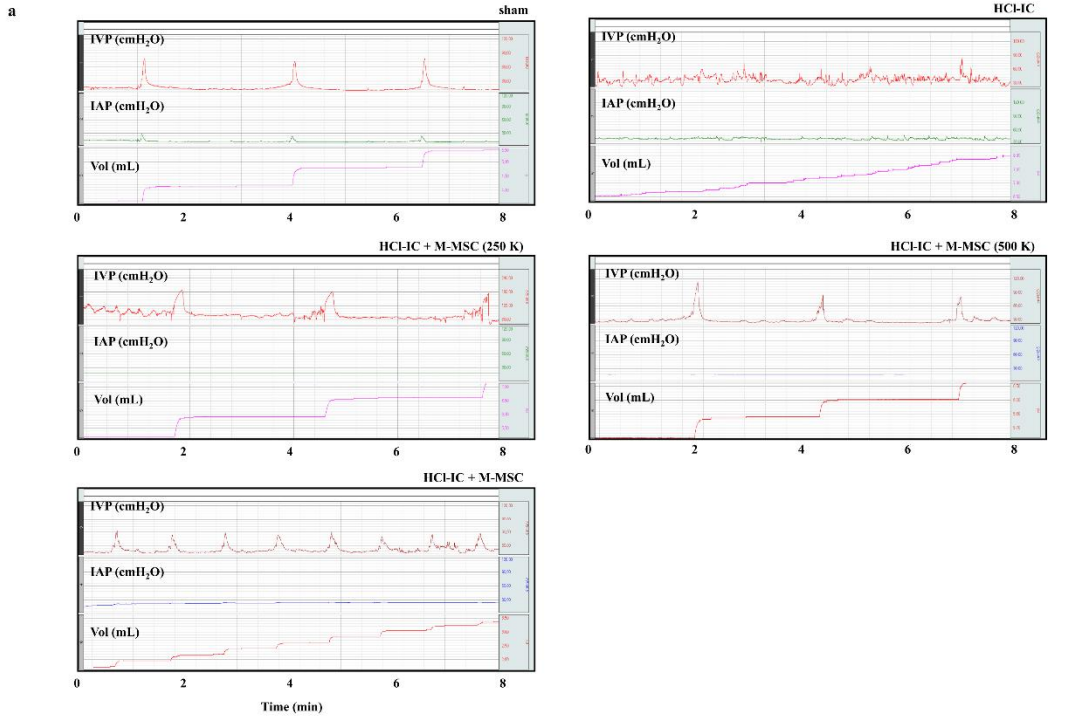


**Figure 1-2. M-MSC injection restored bladder function in HCl-IC model rats.**

(a) Representative awake cystometry results and (b) quantitative bladder voiding parameters at 1 week after the injection of M-MSCs (8 independent animals in each group) at the indicated dosage (K = a thousand). IVP; intravesical pressure, IAP; intra-abdominal pressure. Sham: sham-operated. (c) Quantitative data of bladder voiding parameters at 2 or 4 weeks after the injection of  $1 \times 10^6$  M-MSCs (5 independent animals per group). All data are presented as the mean  $\pm$  SEM, \* $p < 0.05$ , \*\* $p < 0.01$ , \*\*\* $p < 0.001$  compared to the HCl-IC group; # $p < 0.05$ , ## $p < 0.001$ , ### $p < 0.001$  compared to the 1000K group; \$ $p < 0.05$ , \$\$ $p < 0.001$ , \$\$\$ $p < 0.001$  between 2 and 4 weeks group with Bonferroni post-test.

***Evaluation of M-MSC efficacy in bladder tissue.***

Consistent with these functional improvements found in awake cystoscopy, M-MSC of  $2.5 \times 10^5$  or higher resulted in restoration of histological abnormalities in model rats, such as severe adverse effects such as mast cell infiltration, fibrosis and apoptosis (**Fig 1-3a, 1-3b**), which are also characteristic of human IC/BPS bladder<sup>25-28</sup>. However, there was little histological change in the bladder muscle of the rats in all groups.

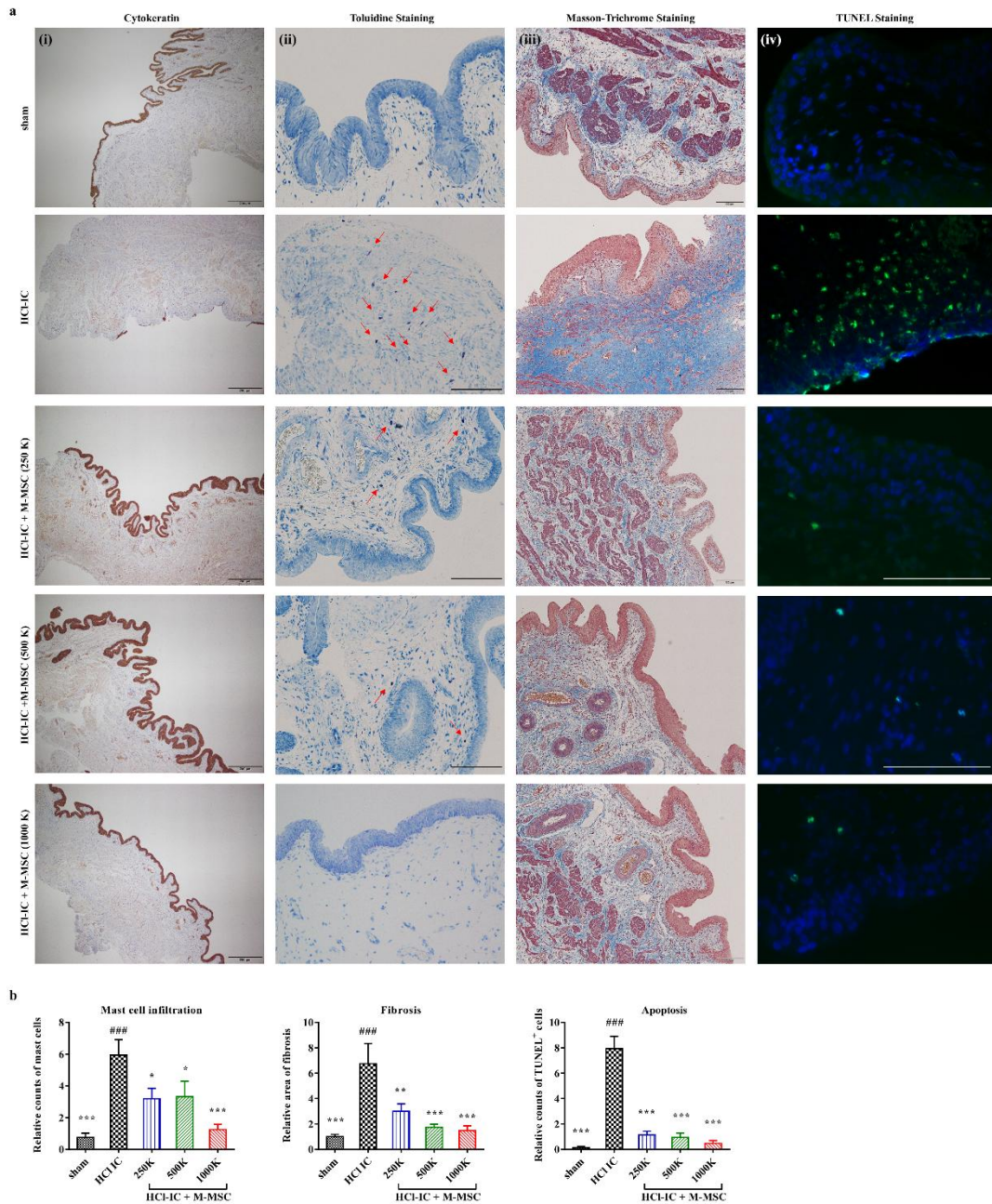


**Figure 1-3. Histological analysis of M-MSC injection effects on HCl-induced bladder injury.**

**(a)** The immunostaining of cytokeratin (i) (magnification  $\times 40$ , scale bar = 100  $\mu\text{m}$ ), Toluidine blue (ii) (magnification  $\times 200$ , scale bar = 100  $\mu\text{m}$ ), Masson's trichrome staining (iii) (magnification  $\times 100$ , scale bar = 100  $\mu\text{m}$ ), and TUNEL assay (iv) (magnification  $\times 400$ , scale bar = 100  $\mu\text{m}$ ) in bladder tissues of HCl-IC rats 1 week after injection of PBS vehicle

or M-MSCs at the indicated dosage (K = a thousand). Arrows indicate infiltrated mast cells. Sham: sham-operated. Nuclei were stained with Mayer's hematoxylin (i, ii, and iii) or DAPI (blue, iv). Arrows (ii) indicate infiltrated mast cells. **(b)** Quantification of histological examinations. Data were normalized to the sham group (n=15). Data are presented as the mean  $\pm$  SEM, \*p<0.05, \*\*p<0.01, \*\*\*p<0.001 compared to the HC1-IC group; #p<0.05, ##p<0.001, ###p<0.001 compared to the 1000K group with Bonferroni post-test.

### ***Effect of M-MSC on visceral hypersensitivity***

IC/BPS patients sometimes experience a variety of other conditions related to pelvic pain including inflammatory bowel syndrome (IBS)<sup>29,30</sup> and communication with internal organs can contribute to the increase of nerve growth factor (NGF), which plays a central role in inflammation, as well as an increased anatomical interaction between symptoms and mast cells and nerve fibers in IC/BPS and IBS patients<sup>31</sup>. Thus, the regenerating structure of the urinary tract epithelium and reduced bladder inflammation after M-MSC treatment can relieve intestinal hypersensitivity of IC/BPS rats. Histological examination of infiltrating mast cells was frequently observed near the nerve fibers in the IC hydrochloride rat bladder; However, the anatomical interactions of mast cells and nerve fibers were markedly reduced by M-MSC treatment (**Fig. 1-4a** and **1-4b**). Furthermore, gene expression analysis indicated that the bladder tissues in IC-HCl rats were characterized by the increased expression of *Ngf* and other genes associated with visceral hypersensitivity such as tumor necrosis factor- $\alpha$  and tachykinin receptor-1; however, the administration of M-MSCs significantly restored their induction in bladder tissues (**Fig. 1-4c**). These results suggest that M-MSC therapy could be beneficial in controlling visceral organ crosstalk as well as the severity and frequency of abdominal pain or discomfort in IC/BPS and IBS patients.

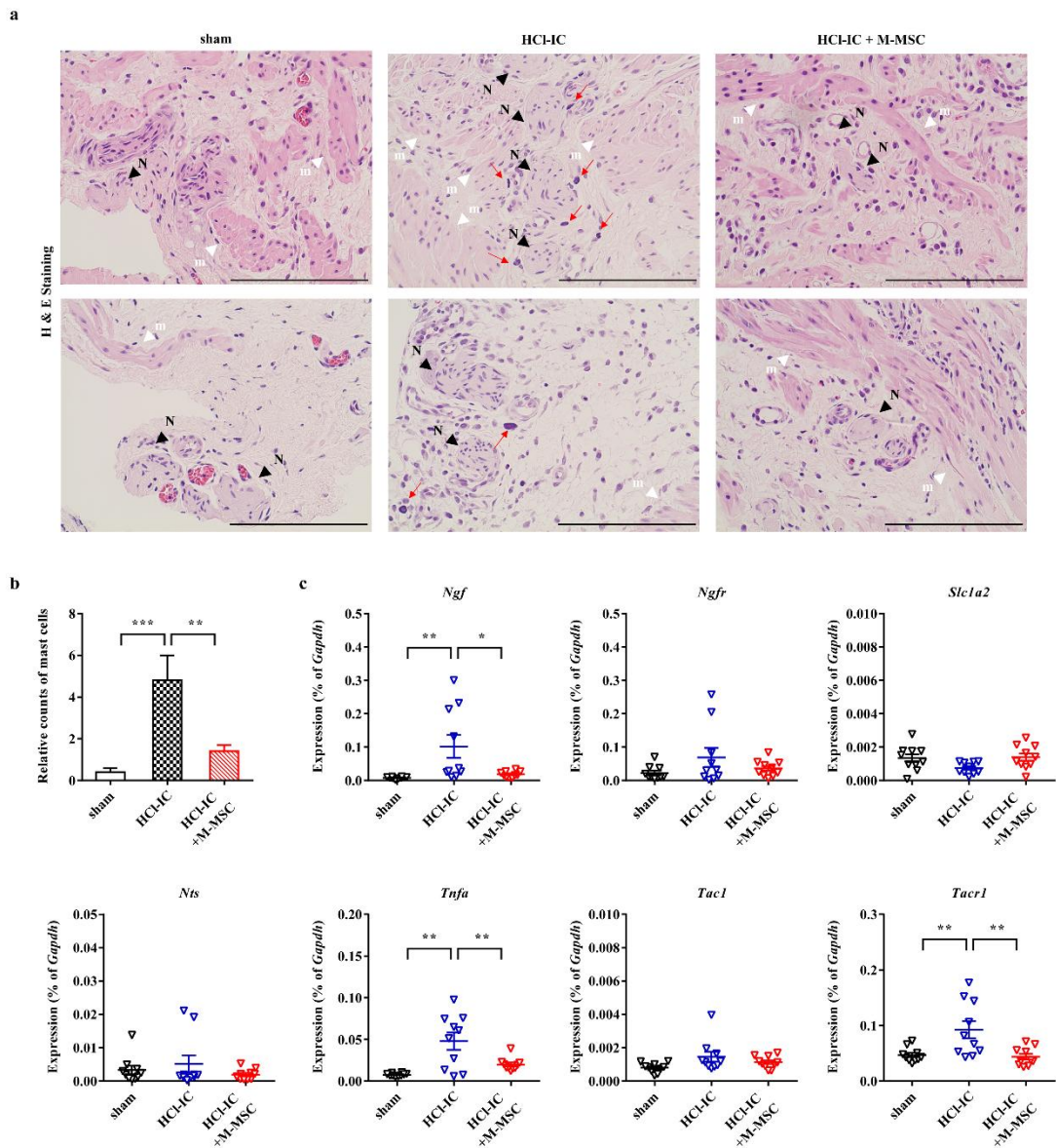


**Figure 1-4. The effect of M-MSC injection on visceral hypersensitivity in HCl-IC model rats.**

**(a)** Hematoxylin and eosin (H & E) staining in the indicated bladder tissues (magnification  $\times 200$ , scale bar = 100  $\mu\text{m}$ ). Nuclei were stained with Mayer's hematoxylin. Arrows indicate the infiltrated mast cells. N (black arrowhead) and m (white arrowhead) indicate the nerve and muscle fibers, respectively. **(b)** Quantification of the mast cells infiltrated around the nerve fibers (n=15). **(c)** RQ-PCR analyses of expression levels of *Ngf* and the genes

associated with visceral hypersensitivity in the indicated bladder tissues 1 week after the injection of  $1 \times 10^6$  M-MSCs or PBS vehicle into HCl-IC animals. Expression is presented as % *Gapdh* (n=10). All data are presented as the mean  $\pm$  SEM, \*p<0.05, \*\*p<0.01, Bonferroni post-test.

***Significance of Wnt and downstream growth factors on M-MSC therapeutic outcome.***

In this paper, to investigate the mechanism of M-MSCs cell therapy for IC/BPSc and investigated the expression of genes related to sonic hedgehog (Shh), Wnt and growth factor by promoting epithelial regeneration in HCI-IC rat model using UCB-MSC therapy<sup>13</sup>. As shown in **Fig. 1-5a**, M-MSC treatment significantly increased Shh and Wnt genes (e.g., *Smo*, *Wnt5a*, *Wnt8a*, *Wnt8b*, *Wnt10a*, and *Wnt11*) as well as their downstream growth factors (e.g., *Igf1*, and *Igf2*), which were characteristically downregulated in bladders of the HCI-IC group. Therefore, the bladder of the HCI-IC+M-MSC group can be characterized by the expression of  $\beta$ -catenin protein, a marker for confirming Wnt signaling activation, and nuclear localization (**Fig. 1-5b** and **Fig. 1-6**). Significantly, the recovery of urinary bladder function was significantly abolished by inhibitors of indomethacin<sup>32</sup> or Gefitinib<sup>33</sup> injection, Wnt and IGF mediated signaling activities (**Fig. 1-5c** and **Fig. 1-7**). The treatment of Gefitinib had little effect on the growth of M-MSC administered to the bladder at the injection site; however, small integrations of injected cells were observed in urothelium (**Fig. 1-5d**). Indomethacin significantly impaired the reproduction of the administered M-MSC. These results demonstrate that the Wnt and IGF signaling pathways play a crucial role in the beneficial outcome of M-MSCs in the treatment of IC/BPS bladder cancer.

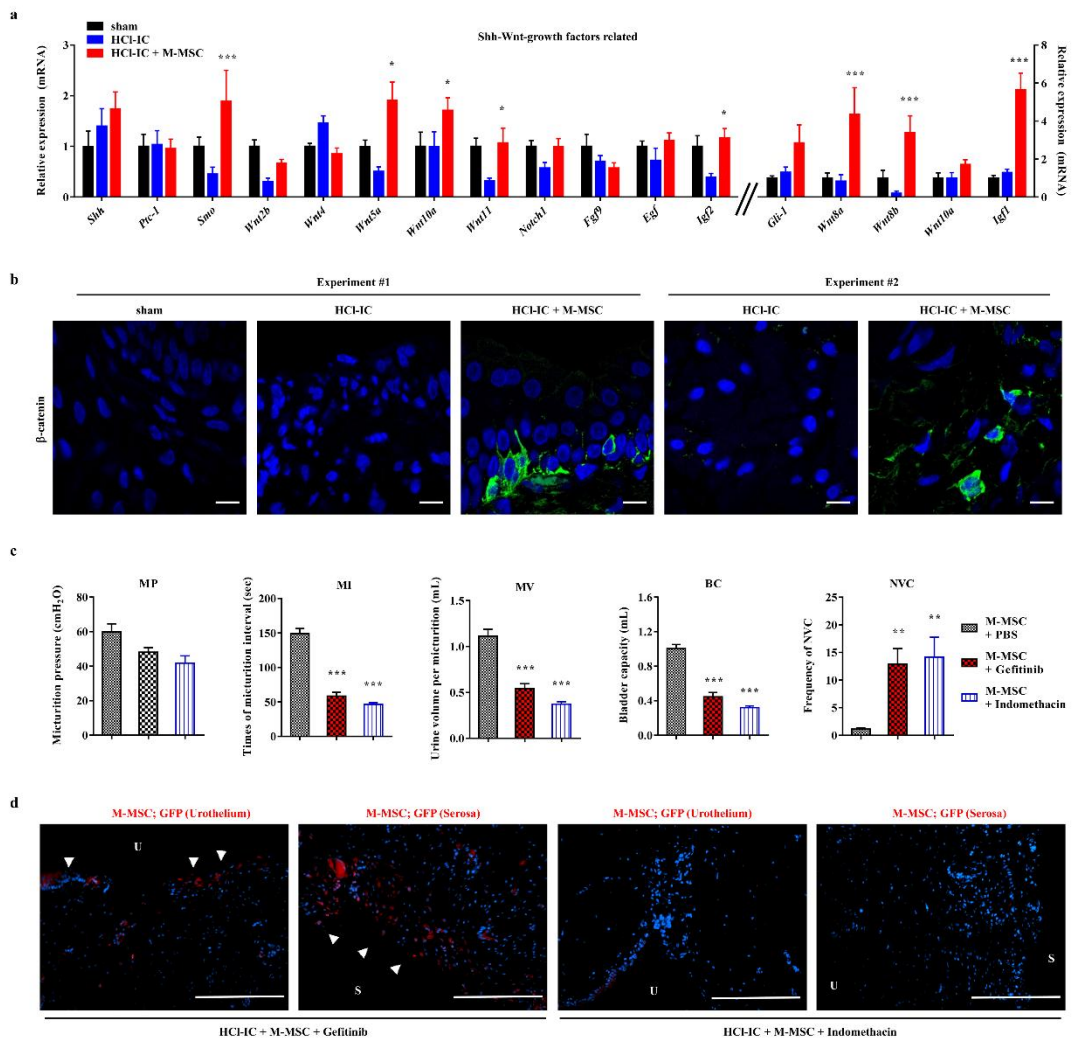


**Figure 1-5. Central role of Wnt and IGF signaling activity on therapeutic effect of M-MSCs.**

**(a and b)** RQ-PCR analyses of expression levels of *Shh*, *Wnt*, and downstream growth factors **(a)** and representative confocal micrographs (magnification  $\times 1,000$ , scale bar=10  $\mu$ m) for immunofluorescence staining of  $\beta$ -catenin protein **(b)** in the bladder tissues of the indicated groups 1 week after the injection of  $1 \times 10^6$  M-MSCs or PBS vehicle into HCl-IC animals. Expression is presented as % *Gapdh* (n=10). **(c)** Quantitative data of bladder voiding parameters in rats (from 8 independent animals per group) at 1 week after the injection of  $1 \times 10^6$  M-MSCs into HCl-IC animals in the absence or presence of indomethacin

(Wnt blocker) or Gefitinib (IGF-mediated signaling inhibitor) intervention. All data are presented as the mean  $\pm$  SEM, \*\* $p < 0.01$ , \*\*\* $p < 0.001$  compared to the HCl-IC group with Bonferroni post-test. **(d)** Detection of M-MSCs stably expressing GFP (red) in the indicated rat bladders by immunostaining (magnification  $\times 200$ , scale bar = 200  $\mu\text{m}$ ). Nuclei were stained with DAPI (blue). Arrow heads indicate the engrafted cells. U; Urothelium, S; Serosa.

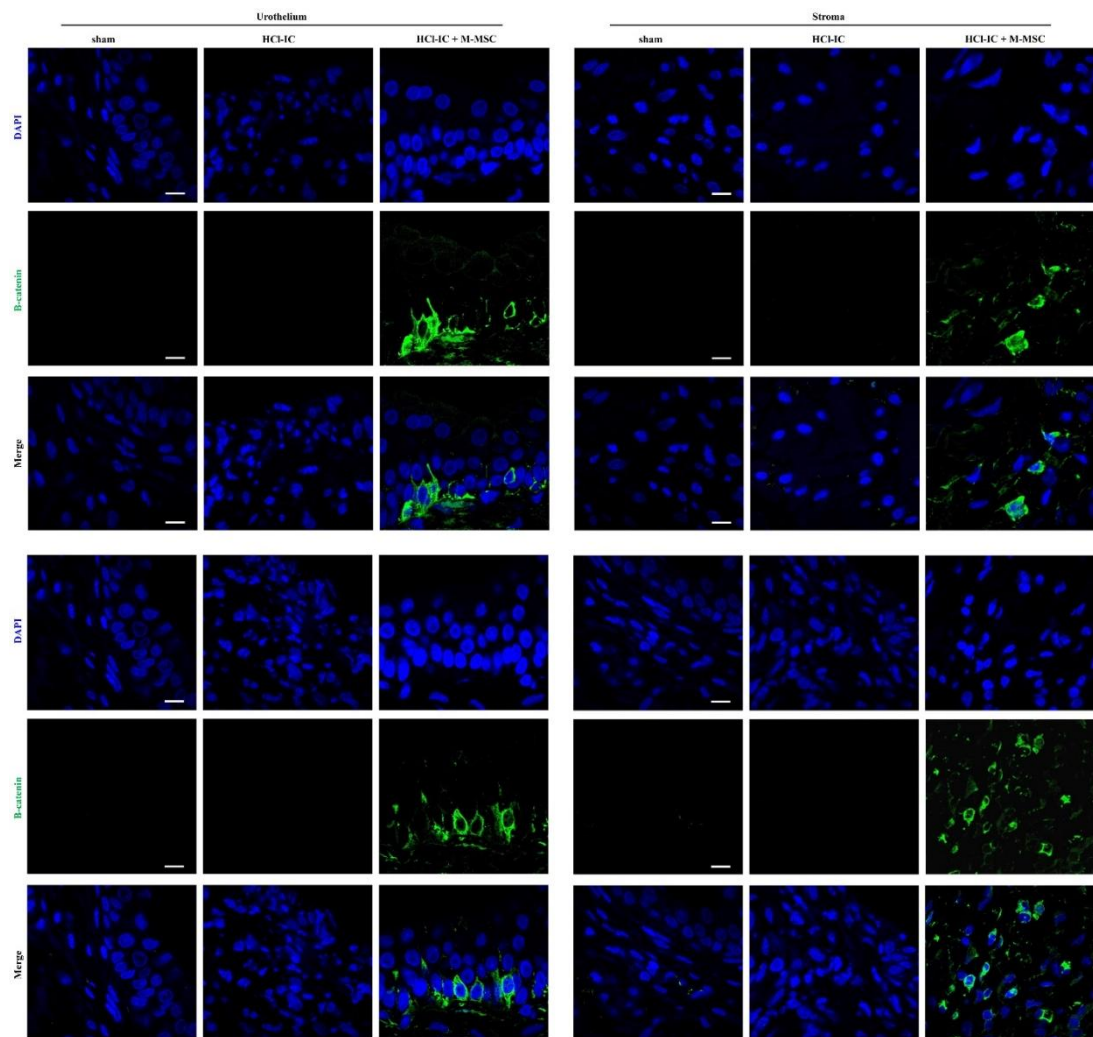


**Figure 1-6. Immunostaining of  $\beta$ -catenin in the bladder after M-MSC therapy.**

Representative confocal micrographs (magnification  $\times 1,000$ , scale bar = 10  $\mu\text{m}$ ) for immunofluorescence staining of  $\beta$ -catenin protein (green) in the urothelium (left panel) and stroma (right panel) sections of bladder tissues at 1 week after the injection of  $1 \times 10^6$  M-MSCs or PBS vehicle into HCl-IC animals. Nuclei were stained with DAPI (blue). Sham: sham-operated.

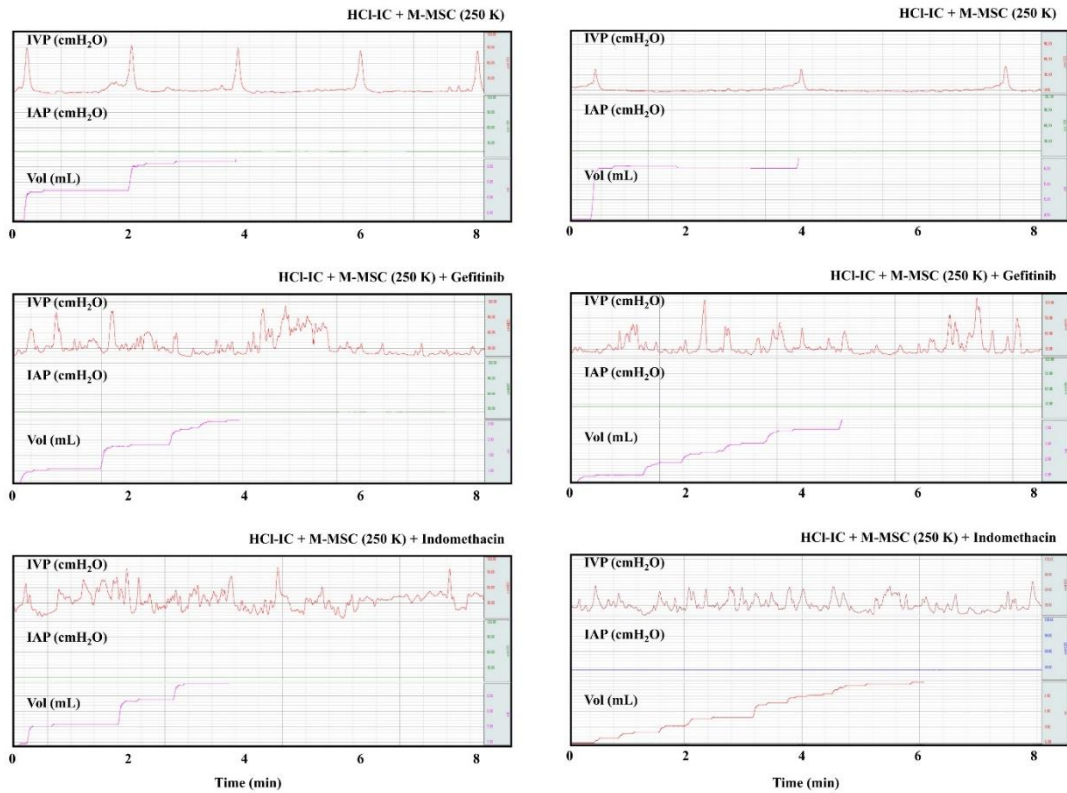


**Figure 1-7. Effect of Wnt or IGF signaling inhibition on M-MSCs therapy for treating HCl-induced IC.**

Representative awake cystometry results in the absence or presence of indomethacin (Wnt blocker) or Gefitinib (used to inhibit IGF-mediated signaling) at 1 week after the injection of  $1 \times 10^6$  M-MSCs into HCl-IC animals (from 8 independent animals per group). IVP; intravesical pressure, IAP; intra-abdominal pressure.

### ***In vivo cellular properties of infused M-MSC***

In immunofluorescent analysis of M-MSCs stably expressing green fluorescence protein (GFP), the majority of GFP<sup>+</sup> cells in HCl-IC animals on 7 DAT were localized at the injection site between muscle and serosa of the bladder and some GFP<sup>+</sup> cells were observed in the lamina propria and urothelium, but few were detected in the muscular layer (**Fig. 1-8a**). In contrast, bladder tissues of rats injected with GFP<sup>+</sup> BM-MSCs showed little GFP<sup>+</sup> grafted cells (**Fig. 1-13**), consistent with the results of bioluminescence analysis (**Fig. 1-9d**). To analyze the phenotypes of transplanted M-MSCs, grafted cells (GFP), E-cadherin, vimentin and endothelial cells (CD31) were labeled and analyzed using a multichannel laser scanning confocal microscope examined. The GFP<sup>+</sup> cells found in urothelium expressed the E-cadherin in membranes showing differentiation into epithelial cells (**Fig. 1-8b** and **1-8c**). Most of the GFP<sup>+</sup> cells found in the lamina propria are distributed as vimentin protein and strong co-staining and stromal cells. In particular, some GFP<sup>+</sup> cells under the serum and urinary tract are distributed in the same vessle-like structure (**Fig. 1-8a**). Confocal microscopy data showed that GFP<sup>+</sup> cells formed in clusters of blood vessels did not express CD31 endothelial cell surface proteins, but were in intimate contact with CD31<sup>+</sup> cells and some expressed vimentin, an intravascular cytoplasm (**Fig. 1-8b**). This perivascular M-MSC phenotype is consistent with previous data in which M-MSCs express surface antigens to pericyte cells (PDGFRB, CD146, and NG2) but not endothelial cells (**Fig. 1-1c**). These results demonstrate that a significant amount of transplanted M-MSCs survives and differentiates into several cell types of bladder tissue.

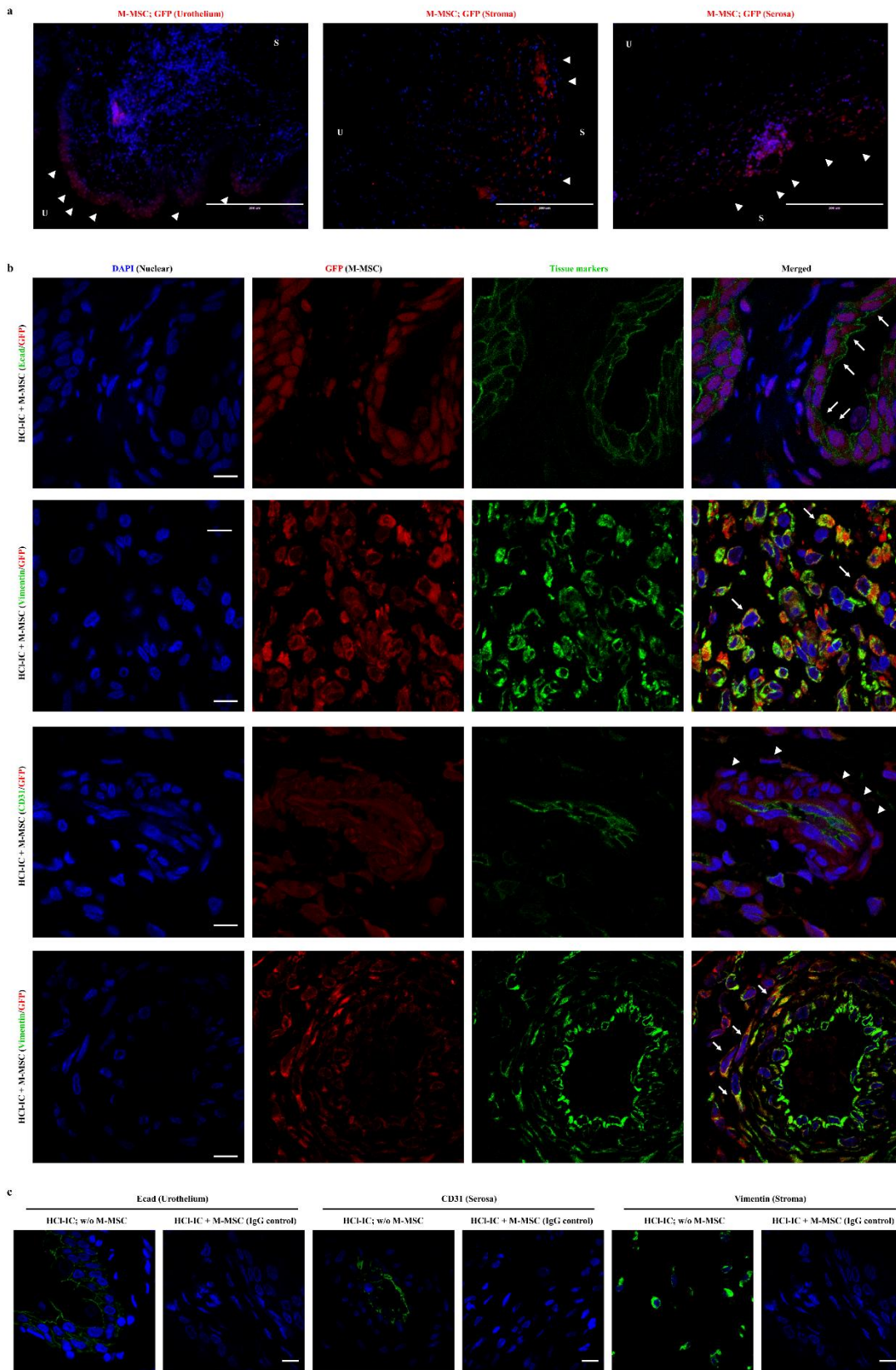


**Figure 1-8. Immunostaining analysis for cellular properties of transplanted M-MSCs.**

**(a)** Detection of M-MSCs stably expressing GFP (red) in HCl-IC rat bladders at 7 DAT by immunostaining (magnification  $\times 200$ , scale bar=200  $\mu\text{m}$ ). **(b)** Representative confocal micrographs of bladder sections transplanted with GFP-MSC (HCl-IC+M-MSC) after double staining for GFP<sup>+</sup> cells (red) and for E-cadherin (Ecad)<sup>+</sup> urothelial cells, vimentin<sup>+</sup> stromal and perivascular cells, CD31<sup>+</sup> endothelial cells (green) (magnification  $\times 1,000$ , scale bar=10  $\mu\text{m}$ ). Nuclei were stained with DAPI (blue). Arrow heads and arrows indicate the engrafted and differentiated cells, respectively. U; Urothelium, S; Serosa. **(c)** For negative control experiments, co-staining of bladders tissues in HCl-IC+M-MSC group animals with mouse and rabbit IgG control antibodies or co-staining of the indicated tissue markers (green) and GFP (red) in bladder tissues not-injected with GFP<sup>+</sup> M-MSCs (HCl-IC; w/o M-MSC) for corresponding tissue markers were included (magnification  $\times 1,000$ , scale bar=10  $\mu\text{m}$ ).

### ***Longitudinal confocal imaging of infused M-MSCs in living animals***

In order to investigate the *in vivo* characteristics of M-MSCs transplanted at the cellular level in living animals (**Fig. 1-9a**), intravital fluorescence microscopy which enables the study of *in vivo* cellular processes such as cell trafficking, intercellular interactions, and vascular changes<sup>36</sup>. Using an front-view endoscopic optical probe for urothelium (**Fig. 1-9b**), study performed longitudinal imaging of GFP<sup>+</sup> M-MSC fluorescence injected for 6-months. Consistent with the optical imaging results, strong focus fluorescence was detected shortly after transplantation into an endoscopy. Fluorescence intensity was significantly reduced by 2 DAT but relatively stable until 21 DAT (**Fig. 1-9c**). During this period, GFP fluorescence was observed in several cellular structures. However, it became weak and blurred beyond 28 DAT. Next, *in vivo* confocal microscopy was performed at high resolution using an objective lens focused on the outer layer of the bladder via minimal incision of the abdominal surface (**Fig. 1-9b**). Fluorescence intensity gradually decreased to 21 DAT. However, GFP<sup>+</sup> cells with clear morphology were still observed at 28 DAT and the release lasted up to 181 DAT. Overall observation period (**Fig. 1-9d**), some auto-fluorescence was observed in animals injected into the vehicle (**Fig. 1-10a** and **1-10b**). In M-MSC-injected animals, star-shaped GFP<sup>+</sup> cells with wide distribution throughout the bladder were detected at 28 DAT (**Fig. 1-9d** and **Fig. 1-10c**). 2-months later, the transplanted cells formed discrete foci and the majority were detected as components of structures such as blood vessels. Similar to the previously described intravital imaging data, confocal microscopy of bladder tissues revealed that grafted M-MSCs functionally integrated into epithelial cells (E-cadherin<sup>+</sup>) in urothelium (**Fig. 1-10d** and **1-10e**) and peripheral vascular cells (vimentin<sup>+</sup> close to CD31<sup>+</sup> cells) and peripheral vascular cell phenotype of M-MSC in 21 DAT (**Fig. 1-9e**) were stable until 6 months (**Fig. 1-9f**). Thus, *in vivo* imaging data suggest that the implanted M-MSCs may initially supplement the urothelial layer and gradually contribute to perivascular cells.

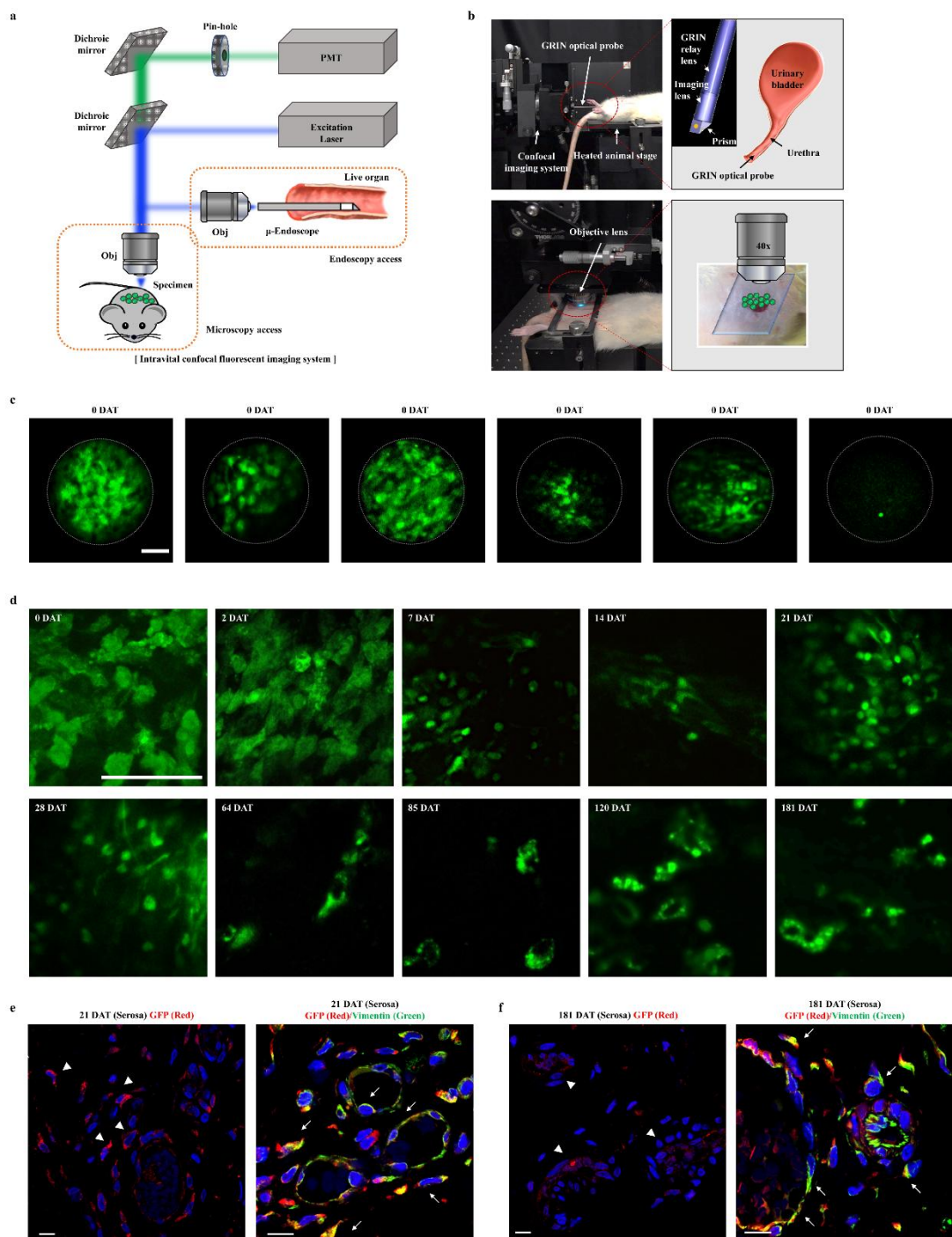


**Figure 1-9. Longitudinal confocal imaging of transplanted M-MSCs in living animals.**

**(a and b)** Schematic overview **(a)** and working station **(b)** of intravital fluorescence imaging in living animal. Front-view GRIN optical probe is endoscopically inserted into the bladder

of an anesthetized rat held on an XYZ stage to access the urothelium surface (**b; upper panel**). Objective lens viewed the outer layer of bladder after making a minimal incision in the overlying abdomen (**b; lower panel**). (**c and d**) Time-lapse imaging (n=8) of the engrafted M-MSCs obtained by a GRIN optical endoscopic probe (**c**, magnification  $\times 40$ ) or objective lens (**d**, magnification  $\times 100$ ) in the bladders of HCl-IC rats from 0 day (2 hours) after transplantation (DAT) to 6 months (181 DAT). A majority of transplanted M-MSCs (with GFP fluorescence) were observed in vascular-like structures in the outer layers of the bladder from about 64 DAT. Scale bar = 50  $\mu\text{m}$ . (**e**) Representative confocal images for integration of transplanted GFP<sup>+</sup> cells (red) (magnification  $\times 630$ ) and their differentiation into vimentin<sup>+</sup> cells near CD31<sup>+</sup> vessels (green) (magnification  $\times 1,000$ ). Arrow heads and arrows indicate the engrafted and differentiated cells, respectively. Nuclei were stained with DAPI (blue). Scale bar=10  $\mu\text{m}$ .

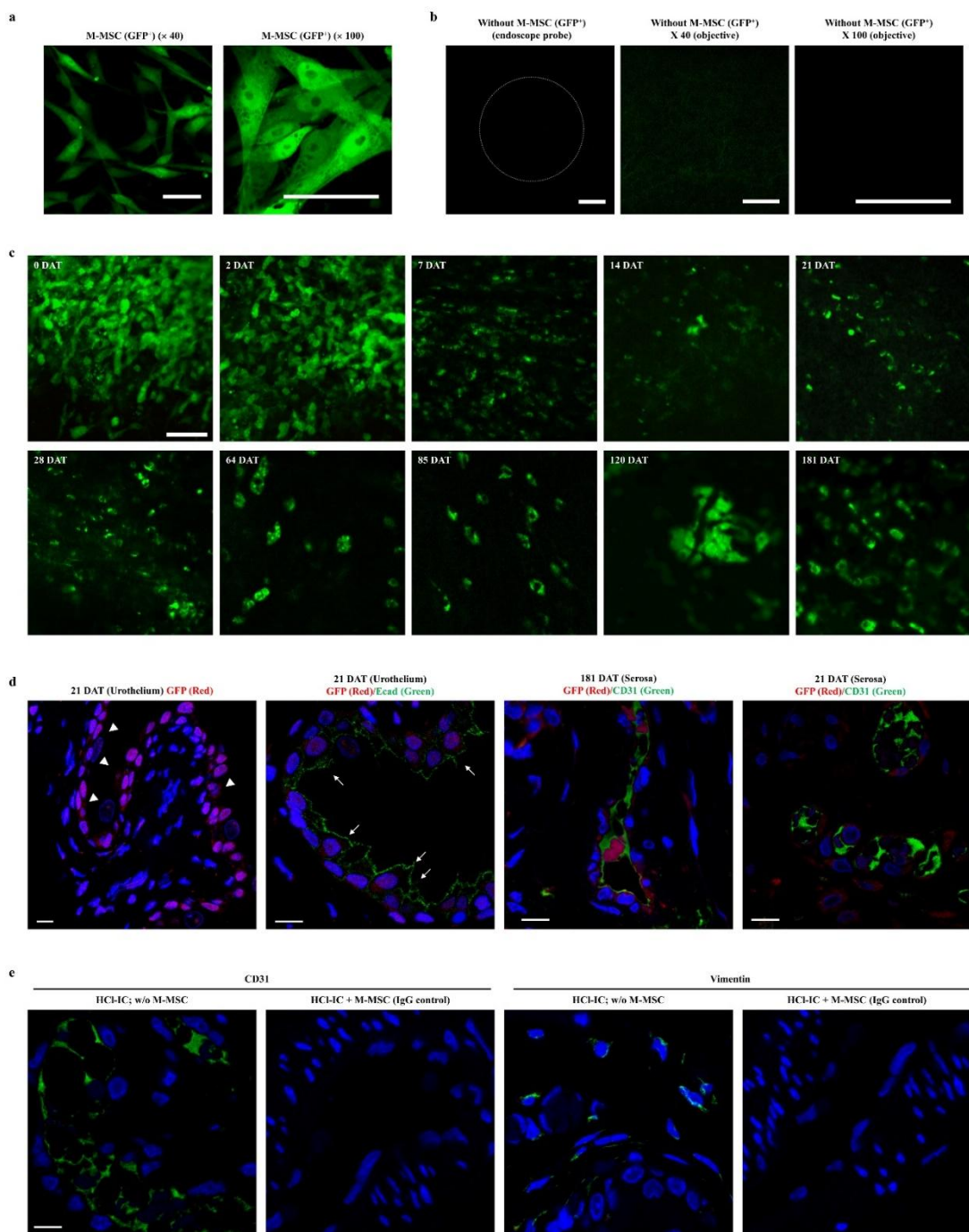


**Figure 1-10. Intravital confocal imaging of the transplanted M-MSCs.**

(a) Representative images for detecting GFP fluorescence during cultivation of GFP<sup>+</sup> M-MSCs (magnification  $\times 40$  and  $\times 100$ ). (b) Only weak fluorescent signals were observed in animals without transplantation of GFP<sup>+</sup> M-MSCs in intravital imaging with an endoscopic

probe (left) or objective lens (middle; magnification  $\times 40$ , right; magnification  $\times 100$ ). **(c)** Longitudinal detection of the engrafted M-MSCs in living animals. Time-lapse images were obtained by objective lens (magnification  $\times 40$ ) over the bladder of HCl-IC rats from 0 day (2 hours) after transplantation (DAT) to 6 months (181 DAT). Objective lene accessed the outer layer of bladder through a minimal incision in the overlying abodomen. Scale bar = 50  $\mu\text{m}$ . **(d and e)** Representative confocal microscopic images for integration of transplanted GFP<sup>+</sup> cells (red) (magnification  $\times 630$ ) and their differentiation into E-cadherin (Ecad)<sup>+</sup> urothelial or CD31<sup>+</sup> endothelial cells (green) (magnification  $\times 1,000$ ) at the indicated DAT **(d)** or for co-staining of bladder tissues in HCl-IC + M-MSC group animals at 181 DAT with mouse and rabbit IgG control antibodies or co-staining of bladder tissues not-injected with GFP<sup>+</sup> M-MSCs (HCl-IC; w/o M-MSC) **(e)**; magnification  $\times 1,000$ ). Nuclei were stained with DAPI (blue). Arrow heads and arrows indicate the engrafted and differentiated cells, respectively. Nuclei were stained with DAPI (blue). Scale bar=10  $\mu\text{m}$ .

### ***Superior therapeutic potency of M-MSCs than adult tissue counterpart***

To compare the efficacy of M-MSCs and adult BM-derived MSCs (BM-MSCs), in this paper, the optimal sub-dose ( $1.0 \times 10^5$  or  $2.5 \times 10^5$ ) of cells to the bladder tissue of HCl-IC. Significantly, M-MSCs showed superior therapeutic efficiency *in vivo* compared to adult tissue counterparts at similar cell doses, and the dose at which BM-MSC did not substantially improve abnormal bladder drainage function, such as MV, BC and MI (**Fig. 1-11a, 1-11b**) were used in IC/BPS model animals. Compared to BM-MSCs, the NVC showing urinary incontinence symptoms was significantly improved in the clinical setting of low dose) ( $1 \times 10^5$ ) M-MSC regimens of M-MSCs (**Fig. 1-11c**).

To obtain the mechanistic insight into the potent efficacy of M-MSCs, the paper describes *in vivo* bioinformatics after transplantation of engineered M-MSCs or BM-MSCs capable of stably expressing enhanced Renilla luciferase and Venus chimeric Nano-lantern Fluorescent proteins with high efficiency of bioluminescence resonance energy transfer (BRET) were used<sup>34</sup>. To optimally monitor the bioluminescence signal of the transplanted cells, a rat model in which IC/BPS was induced by CYP<sup>35</sup> was used and a  $2 \times 10^5$  Nano-lantern<sup>+</sup> M-MSCs or BM-MSCs was injected locally into the bladder tissue. The bioluminescence intensities of the implanted M-MSCs were observed through an optical imaging system up to 8 days post-transplant (DAT) (**Fig. 1-12**).

After a rapid decrease ( $\sim 5\%$  compared to when cells were injected) in 1 DAT, the bioluminescent activity of the grafted M-MSC persisted to 4 DAT and significantly decreased after 7 DAT (**Fig. 1-11d**). Compared to BM-MSC treated animals, the animals transplanted with M-MSC exhibited significantly bright bioluminescence during the whole experimental period (**Fig. 1-11d**), indicating excellent engrafting ability of M-MSC. The paper monitored the tumor formation of non-invasively implanted M-MSCs using tumor micro-positron emission tomography/magnetic resonance imaging (MRI) imaging for 12 months post-injection. The paper monitored the tumor formation of non-invasively

implanted M-MSCs using tumor micro-positron emission tomography/magnetic resonance imaging ( $\mu$ -PET/MRI) imaging for 12 months post-injection (**Fig. 1-14**). As shown in Fig. 10, only background signals for ingestion of 2- $^{18}\text{F}$ -fluoro-2-deoxyglucose (FDG) was detected, and no other  $^{18}\text{F}$ -FDG absorption characteristics were observed.  $1 \times 10^6$  M-MSC or PBS vehicle was injected. And confirmed the possibility of tumorigenesis of M-MSC through thorough microscopic examination of the organ in double-blind necropsy and final nanoScanPET/MRI analyzes. Taken together, these results suggest that M-MSC-based therapies with no adverse side effects or safety can provide superior therapy and viability for the treatment of IC/BPS bladder dysfunction by supporting Wnt signal epithelial regeneration.

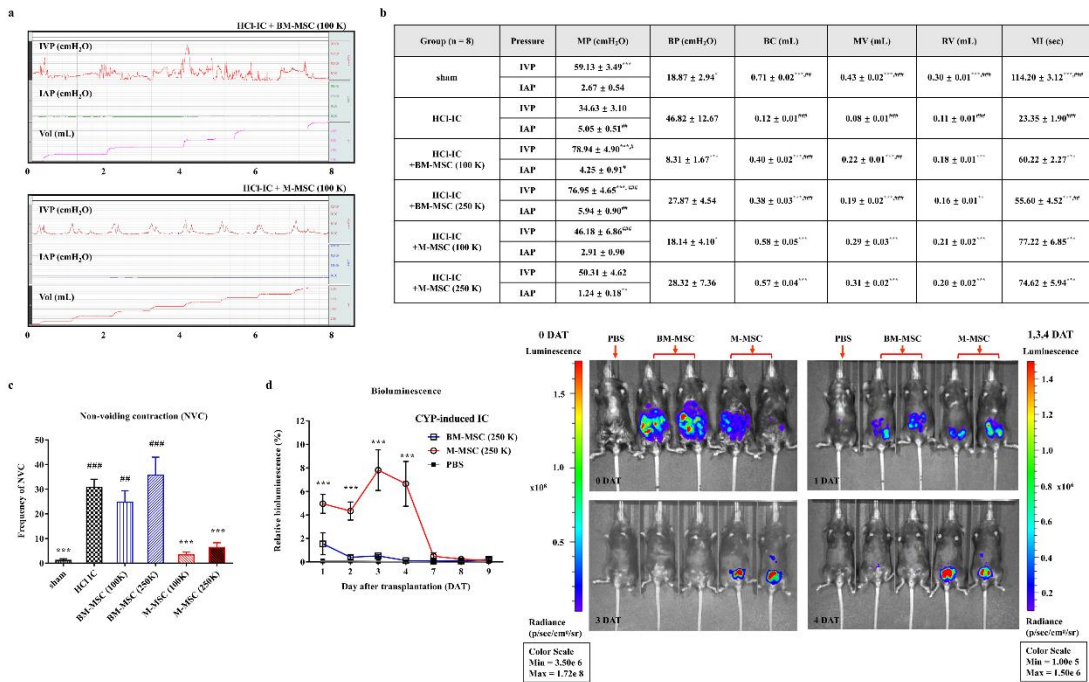


**Figure 1-11. Superior therapeutic efficacy of M-MSCs compared to BM-MSCs.**

**(a)** Representative awake cystometry results at 1 week after injection of M-MSCs or BM-MSCs at the indicated dosage (K = a thousand) into the bladder of HCl-IC rats. **(b)** The micturition pressure (MP), basal bladder pressure (BP), bladder capacity (BC), micturition volume (MV), residual volume (RV), and micturition interval (MI) were quantified from the voiding pattern analysis. **(c)** Quantification of non-voiding contraction (NVC) in HCl-IC animals transplanted with the indicated number of M-MSCs or BM-MSCs (n=8). All data are presented as the mean ± SEM from 8 independent animals per group (\*p<0.05, \*\*p<0.01, \*\*\*p<0.001 compared to the HCl-IC group; #p<0.05, ##p<0.001, ###p<0.001 compared to M-MSC (250K) group by one-way analysis of variance with Bonferroni post-test). **(d)** The time course of viability of transplanted M-MSCs or BM-MSCs ( $2.0 \times 10^5$ ) in cyclophosphamide (CYP)-induced IC/BPS mice. Relative bioluminescent signals for the indicated day after transplantation (DAT) relative to 0 DAT are presented as the mean ± SEM (n=5; \*\*\*p<0.001 compared to the BM-MSC group). The representative images were

obtained at 15 minutes after intraperitoneal injection of 150  $\mu\text{g/ml}$  coelenterazine (200  $\mu\text{L}$ ), a substrate for Renilla luciferase. The scale bars for optical image density range at 0 and other day points were presented at left and right sides of image, respectively.

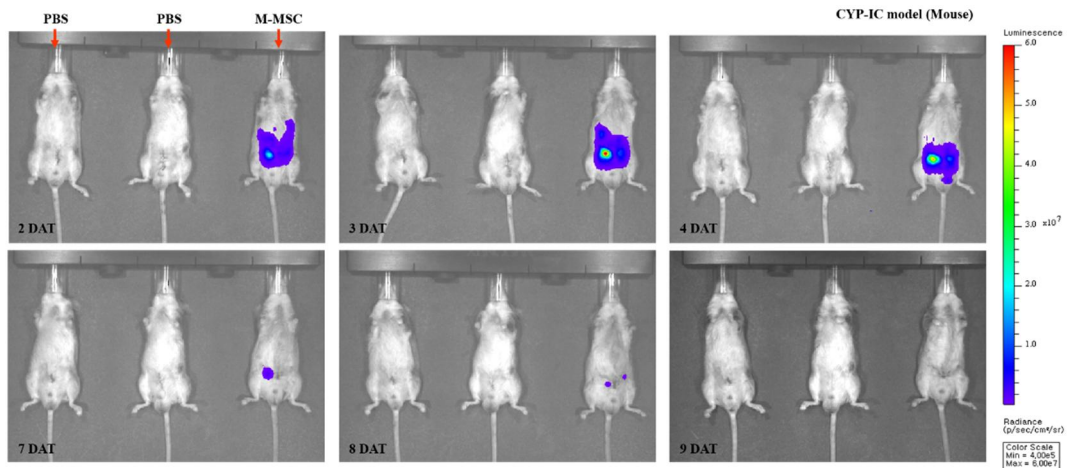


**Figure 1-12. Bioluminescence assay of transplanted M-MSCs.**

Imaging of bioluminescence activities from injected M-MSCs at the indicated day after transplantation (DAT). The representative images were obtained at 15 minutes after intraperitoneal injection of 150  $\mu\text{g/ml}$  coelenterazine (200  $\mu\text{L}$ ), a substrate for Renilla luciferase. PBS vehicle or  $2 \times 10^5$  Nano-lantern expressing M-MSCs or BM-MSCs were administered directly into bladders of a murine model of IC/BPS induced by intraperitoneal administration of cyclophosphamide (100 mg/kg) every two days for one week.

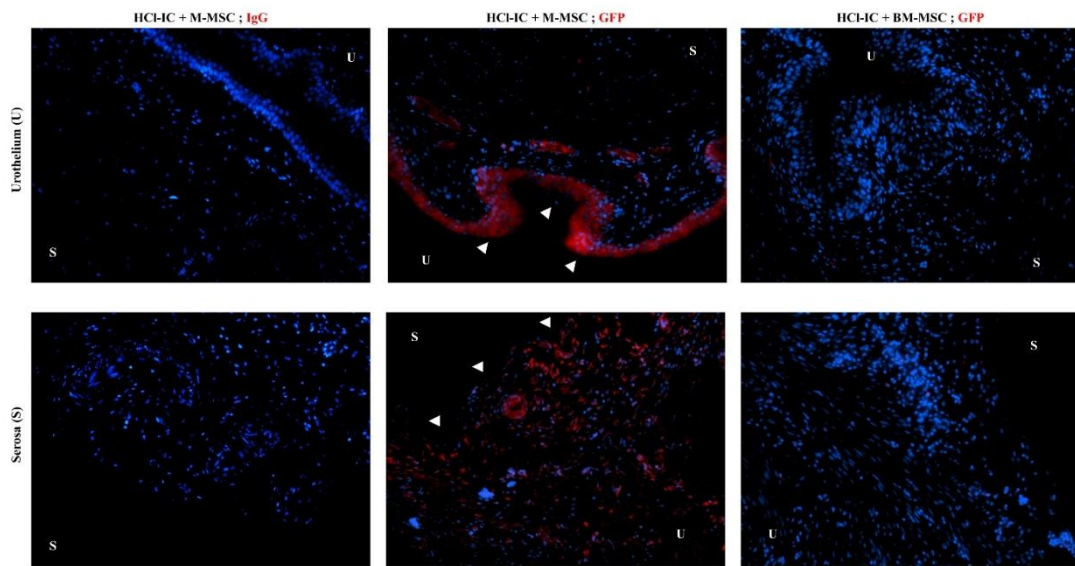


**Figure 1-13. Limitation of BM-MSCs about in vivo engraftment.**

Immunofluorescence staining of GFP for detection of the injected GFP<sup>+</sup> BM-MSCs in HCl-IC rat bladders at 7 days after transplantation (magnification  $\times 200$ ). Nuclei were stained with DAPI (blue).

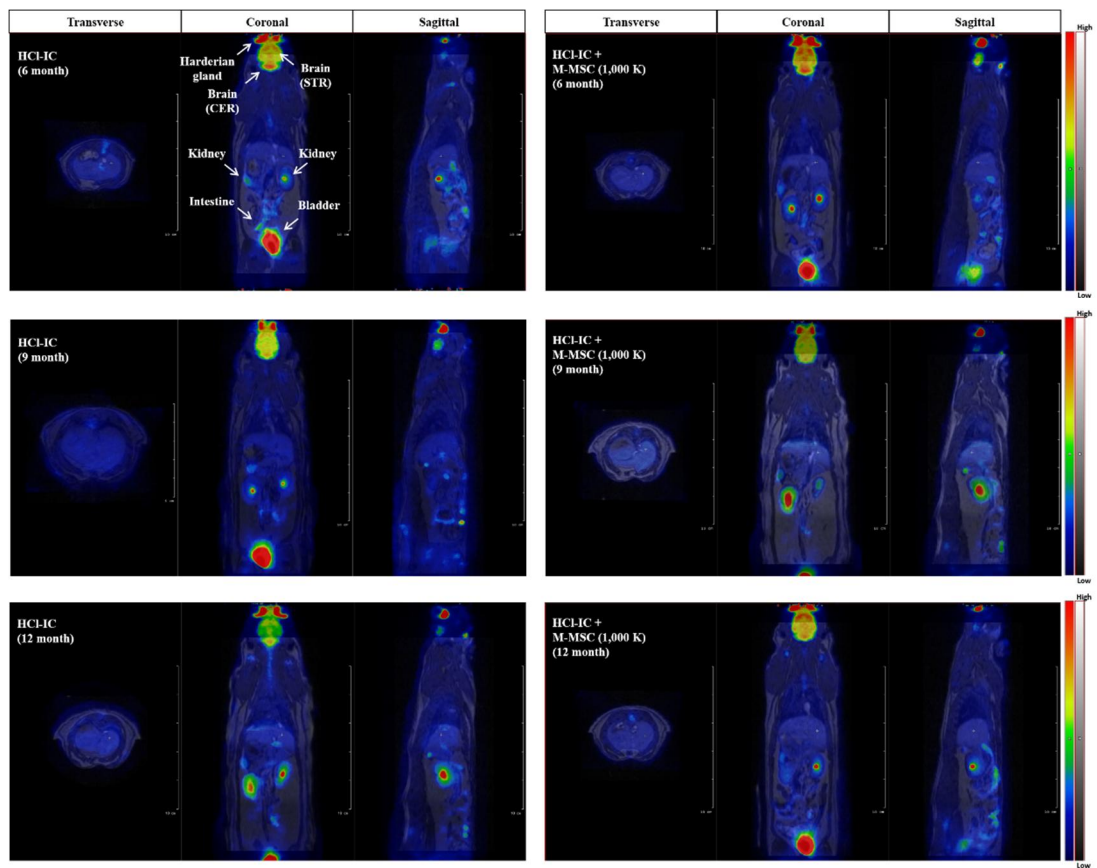


**Figure 1-14. micro-PET/MRI imaging assay of transplanted M-MSCs.**

Longitudinal PET/MRI imaging of transplanted M-MSCs. The transverse, coronal, and sagittal views of fused MRI (T1 GRE EX) and PET images (15 min scan after [<sup>18</sup>F]-FDG injection) of HCl-IC rats at 6, 9, and 12 months after injection of PBS vehicle (left) or transplantation of  $1 \times 10^6$  M-MSCs (right, HCl-IC + M-MSCs) (n=5).

## DISCUSSION

Several promising preclinical studies using MSCs to treat IC/BPS have been reported, but skepticism about current MSCs-based therapies has spurred due to limited information on *in vivo* characteristics of transplanted cells as well as limited proliferation and damaged stems during *in vitro* expansion. To overcome these limitations, the results of IC/BPS treatment without safety problems in animal models compared to adult tissue-derived cells *via* injection of hESCs-induced M-MSCs and the use of hESCs as a virtually unlimited source of MSCs. It also provides accurate information on the *in vivo* distribution and cellular characteristics of the transplanted cells through a confocal microscope, within a living animal model.

IC/BPS is considered to be a heterogeneous multifactorial disease with an unknown pathogenesis<sup>37</sup>. The etiology of the disease is not fully understood, and no definitive treatment has been reported. Several treatments have been introduced, including various oral medications, bladder instillation therapies, fulguration for Hunner's lesions and hydro-distention but only unsatisfactory results have been reported. IC/BPS may be a chronic inflammatory and fibrotic disease that affects the entire bladder due to mast cell activation, increased sensory nerve activity, nitric oxide or autoimmune mechanisms, and a glycosaminoglycan layer. And suggests that an approach to multi-modal therapy may be needed<sup>38-40</sup>. For this purpose, SC therapy has several advantages, and indeed MSC-based therapy has proven beneficial in preclinical studies by regenerating damaged tissues through differentiation into target cells and creating a micro-environment favorable to tissue repair<sup>12-</sup>

14.

For reference, nearly 40% of patients diagnosed with IC, and 40% of patients diagnosed with IBS as symptoms of bladder pain, had symptoms that met the criteria for ICB<sup>29, 30</sup>. Intrathoracic communication acquired hypersensitivity can be attributed to the fusion of the

posterior ganglion neural sensory pathway, spinal cord and brain<sup>41</sup>. Other evidence showed hypersensitivity of centrilobular nerve cells as well as celiac nerves in dorsal root ganglia following hyperintense inflammation<sup>31</sup>. Thus, activation of afferent nerves responsive to mucosal injury may be the result of increased epithelial permeability, which allows the electrolyte to directly access the visceral sensory neurons. In this regard, the attenuation of inflammation and structural regeneration by M-MSC therapy can prevent the internal organs crosstalk. Accordingly, it was confirmed that a single administration of M-MSCs significantly alleviated the anatomical interactions between mast cells and nerve fibers (**Fig. 1-4a** and **1-4b**). And expression of Ngf was increased in both mast cells and nerve fibers (**Fig. 1-4c**). Therefore, the evaluation of pain after treatment of M-MSCs in the intestinal inflammatory state should be conducted at a later stage. Single doses of hESC-derived M-MSCs showed therapeutic effects in HCI-induced IC animal models (**Fig. 1-2**), consistent with previous studies using UCB-MSCs. The transplanted cells are vimentin<sup>+</sup> stromal cells (**Fig. 1-8a**, **1-8b**, and **Fig. 1-9e**) capable of stimulating Wnt-related epithelial regenerative capacity (**Fig. 1-5**), localized mainly between the muscles and the serosa, and sparse in the thin fascia. Significantly, the transplanted M-MSCs yielded beneficial results, even when the injected cells were 10-fold less than the BM-MSCs treated in the HCI-IC animal model (**Fig. 1-11**). This critical potency has been shown to enhance viability *in vivo* (**Fig. 11d**) and is an important challenge for MSCc-based therapies in adult tissues<sup>42</sup>. In previous reports, most (99%) veins attached to the lungs and a mere 2–3% were released by injected MSCs<sup>43</sup>. Similarly, about 5% of locally injected M-MSCs were detected in the bladder tissue of 1 DAT (**Fig. 1-11d**). However, intravital imaging analysis in this study confirmed that some M-MSCs were injected stably into the damaged bladder and survived for at least 6 months (**Fig. 1-9d** and **Fig. 1-10c**). As a result, GFP<sup>+</sup> cells transplanted from the bladder of IC/BPS animal models were detected as vimentin<sup>+</sup> stromal cells or pericytes as well as E-cadherin<sup>+</sup> urothelium (**Fig. 1-9e** and **Fig. 1-10d**). Stable integration of transplanted cells as naive

urothelium, stromal, and perivascular cells can maximize therapeutic potential by protecting the bladder from urinary leakage and enhancing the progenitor microenvironment. In addition, the infinite proliferative capacity of hESCs can be provided as a quality therapeutic cell through *in vitro* differentiation characteristics that improve *in vivo* survival, growth and function<sup>23</sup>. Despite these advantages, one risk in the treatment of hESC-derivatives is the possibility of tumorigenesis. However, the successful outcome of eye diseases discovered in recent clinical studies may be of interest to hESCs-based therapies<sup>44, 45</sup>. Similarly, long-term longitudinal nanoScanPET/MRI monitoring and thorough testing in tumor and organ transplanted M-MSCs did not reveal abnormal growth (**Fig. 1-14**). In addition, no signs of immunodeficiency or inflammation were observed during the experiment. hESCs and differentiated derivatives<sup>46, 47</sup> may have low immunogenicity because they do not have an immunologically relevant surface surface marker, including HLA-DR (**Fig. 1-1c**) and co-stimulatory molecules (CD40, CD40L, B7-1 and B7-2)<sup>24</sup>, which may enable M-MSCs to migrate out of the immune response and be transplanted in perivascular cells for a long term. Taken together, clinical data from this study show that hESCs-derived M-MSCs can overcome the limitations of MSCs therapy, which have been known to date, without the deleterious consequences of hESCs derivatives. In a recent study, several priming strategies have been developed to enhance the function of MSCs derived from adult tissues<sup>48-50</sup>. Thus, the therapeutic effect and expansion of M-MSCs as compared to the results of MSCs should be thoughtful, easily accessible, and related to clinical applications. Important limitation of clinical SC therapy is the depletion of direct long-term analysis of distribution, phenotypes and functional integration of transplanted cells in injured target organs. Functional characteristics that are important in transplanted SCs include transcriptional activity, external signaling and differentiation, which dynamically change depending on the disease setting and affect the outcome of treatment<sup>51</sup>. Thus, *in situ* analysis of cells transplanted into living animals will enhance understanding of cellular mechanisms and better assess the risk of

tumors and other adverse events that can occur after cell transplantation, thus helping to develop optimal treatment protocols. Preclinical results based on these data can lead to successful clinical trial results. The present study longitudinally examined the cellular processes of M-MSCs transplanted into tumors for 6 months (**Fig. 1-9**). In this paper repeatedly visualized various cell-level processes using a high-resolution objective lens (**Fig. 1-9d**). However, large-sized objective lenses have been limited to surface tissues such as the skin and the externally exposed inner surface. To overcome this drawback, endoscopy was used with a small diameter refractive index (GRIN) lens probe, which is a noninvasive method for visualizing intact tissue (**Fig. 1-9b**). Surprisingly, similar patterns of fluorescence signals were observed when using two approaches. However, the endoscopic approach was able to trace the transplanted cells only within the 28 DAT (**Fig. 1-9c**), but was also visualized under the objective lens at the 181 DAT (**Fig. 1-9d**). This discrepancy in detection may be due to the limited optical penetration depth of the GRIN probe, which is only about 100 mm in soft tissues<sup>36</sup>. It is important to note that most of the transplanted cells were observed in the form of multiple cells on the surface of the bladder until 1 month after injection, but they were distributed locally until 2 months after transplantation (**Fig. 1-9d**). Thus, it can be assumed that the implanted M-MSC initially replenishes the Urothelial layer and gradually establishes a microenvironment favorable for tissue repair. Specific promoters and multiple lineages are needed for better insight. With the rapid development of SC research, successful clinical application of SC treatment in urology is expected in the near future<sup>12, 52, 53</sup>. In order to obtain a successful preclinical study, this paper suggests that hESC-derived M-MSC is an ideal, efficient, and efficient source of therapeutic cells with improved potency and minimal tumorigenesis and immunogenicity. Currently known is the first study to longitudinally characterize the characteristics of SCs transplanted at the cellular level of living animals. This innovative approach can overcome the limitations of current SC therapy and improve understanding of SC therapy mechanisms.

## **CHAPTER 2**

### **Development of reliable chronic bladder ischemia rat model for reproducing the detrusor underactivity**

## INTRODUCTION

Detrusor underactivity (DUA) is defined as reduced detrusor contraction strength and/or duration, resulting in prolonged bladder emptying and/or failure to achieve complete bladder emptying within a normal time span<sup>58</sup>. DUA is a frustrating diagnosis for clinicians as well as patients since no effective pharmacological treatment is available<sup>60, 61</sup>. To date the only treatment option has been lifelong clean intermittent catheterization (CIC) with the attendant risk of urethral laceration, recurrent urinary tract infection, occasional bladder perforation, and possible deteriorating renal function<sup>61, 62</sup>. In addition, the socioeconomic and psychological burdens of lifelong CIC must be considered<sup>63, 64</sup>. Annually, neurogenic bladder patients have on average 16 office and 0.5 emergency room visits in the United States<sup>64</sup>.

The prevalence of urodynamically confirmed DUA in elderly patients with lower urinary tract symptoms (LUTS) is approximately 28.0% (40.2% in males and 13.3% in females), and the prevalence of DUA increases with age<sup>65</sup>. Vascular endothelial damage (VED) also occurs during the human aging process and is an independent risk factor for atherosclerosis and hypertension<sup>65</sup>. Pelvic arterial insufficiency, a common clinical problem in elderly population, may lead to impaired lower urinary tract perfusion and has an important role in voiding dysfunction, such as DUA or detrusor overactivity (DO).

Animal models reproducing DUA are scarce. Studies in a rabbit model of chronic bladder ischemia (CBI) suggested that moderate ischemia causes DO<sup>67</sup>, while severe ischemia causes bladder DUA<sup>68</sup>. Similar findings were also observed in a rat model<sup>69</sup>. Nomiya et al. reported that progressive VED may lead to bladder DUA in rats<sup>69</sup>. However, previous CBI-induced DUA rat models have some limitations. First, the pattern of the voiding function induced in the CBI rat model was so varied as to be unpredictable. The

previous CBI rat model induced DUA<sup>69, 70</sup>, but it also induced OAB in the same study settings<sup>71</sup>. Second, previous studies have utilized artificial agents such as a nitric oxide synthase inhibitor (L-NAME) in the rat model to enhance the vascular intimal changes<sup>71</sup>. Lastly, the pathophysiology of CBI-induced DUA was not fully elucidated in previous studies<sup>69, 70</sup>.

Considering the above, this study attempted to establish a more reliable DUA rat model. This study hypothesized that sufficient physical damage for VED, without any enhancers, is sufficient to induce DUA. This study investigated the effects of the severity of CBI on voiding behavior and bladder function in rat models. Moreover, genome-wide gene expression profiling was carried out to identify molecular pathways strongly associated with the pathogenesis of CBI-induced DUA.

## **MATERIALS AND METHODS**

### ***Ethics statement and study approval***

All animal experiments were approved and performed in accordance with guidelines and regulations of the Institutional Animal Care and Use Committee of the University of Ulsan College of Medicine (IACUC-2018-12-145).

### ***Chapter 2. Study Design***

Male 16-week old Sprague–Dawley rats were divided into control (n=12), sham (n=12), and arterial injury (AI) groups treated 10 (AI-10; n=13), 20 (AI-20; n=12), and 30 times (AI-30; n=10). The AI-10, AI-20, and AI-30 groups were subjected to the following procedure to induce VED of the bilateral iliac arteries using a 2-French forgartic catheter (Fig. 1A). Sham, AI-10, AI-20, and AI-30 groups received a 1.25% cholesterol diet (D12336, Research Diets). After 8 weeks, all rats underwent 24-hour voiding pattern analysis and unanesthetized cystometrogram. Thereafter, bladder tissues and iliac arteries were processed for organ bath investigations, immunohistochemistry staining, and gene expression analysis.

### ***Analysis of 24-hour voiding pattern***

Twenty-four hours of natural voiding patterns in the metabolic cage were recorded and analyzed using Acq Knowledge 3.8.1 software and an MP150 data acquisition system (Biopac Systems, Goleta, CA, USA) at a sampling rate of 50 Hz.

### ***Unanesthetized and unrestrained cystometrogram***

The evaluation was performed in the awake state with an unrestrained animal model in metabolic cages. Intravesical pressure (IVP) and intraabdominal pressure (IAP) were recorded 3 days prior to the cystometrogram, as described in elsewhere<sup>55-59</sup>. The urethra was

approached using a PE-50 catheter (Clay Adams, Parsippany, NJ) connected to a pressure transducer (Research Grade Blood Pressure Transducer, Harvard Apparatus, Holliston, MA, USA) and a microinjection pump (PHD22/2000 pump, Harvard Apparatus). Voiding volumes were recorded by means of a fluid collector connected to a force displacement transducer (Research Grade Isometric Transducer, Harvard Apparatus) as normal saline was infused into the bladder at a rate of 0.4 mL/min. The IVP and IAP were recorded continuously. The mean values from three reproducible voiding cycles using individual animals were used for evaluation. Maximum pressure was defined as the maximum IVP during the micturition cycle. The micturition pressure was defined as the maximum IVP subtracted by IAP during the micturition cycle. The micturition volume (MV) was the volume of expelled urine, and residual volume (RV) as the urine volume remaining following voiding. RV was measured by aspiration of residual urine using the PE-50 catheter immediately after urination. Bladder capacity (BC) was estimated by the summation of MV and RV.

***Organ bath study.***

Longitudinal strips of the posterior wall of the bladder dome were mounted in organ baths (5 mL) containing Krebs solution and bubbled with 5% CO<sub>2</sub> and 95% O<sub>2</sub> (37°C). One hook was suspended from a transducer (type 45196 A; San-ei Instruments, Tokyo, Japan), and the lower hook was fixed to a plastic support leg attached to a micrometer (Mitutoyo, Tokyo, Japan). Each strip was equilibrated unstretched for 40 minutes. A load of 2.0 g was applied to each strip by micrometer adjustment and the load was readjusted to this level 30 minutes later. Changes in the tone of the strips were measured isometrically using force transducers and the data were recorded using LabChart v7.3.8 software and a PowerLab/16sp data acquisition system (AD Instruments, Castle Hill, Australia). Contractions by the KCl (P9333; Sigma-Aldrich; 80 mM), ATP (A2383; Sigma-Aldrich; 1mM), electrical field stimulation

(EFS; 1, 2, 4, 8, 16, and 32 Hz), and carbachol (PHR1511; Sigma-Aldrich; 1 nM to 1 mM) were recorded. All bladder strips were normalized to weight per 1 g.

### ***Histologic examination***

The iliac artery thickness of each groups were quantified. Mast cell and collagen infiltration in muscle layer were assessed using toluidine blue staining (toluidine blue-O, Daejung Chemicals & Metals Co.) and Masson's trichrome staining (Junsei Chemical, Tokyo, Japan), respectively. The presence of peripheral nerves in the bladder muscle layer was assessed by N,N-dipropyl-2-[4-methoxy-3-(2-phenylethoxy)phenyl] ethylamine staining (SML0631; NE-100, Sigma-Aldrich). In addition, anti-alpha smooth muscle actin antibody staining (ab7817; Mouse mAb 1A4, Abcam) was performed to evaluate the bladder muscular atrophy. Apoptosis of the bladder mucosa and muscle layer was assessed by terminal deoxynucleotidyl transferase dUTP nick-end labeling staining (1 684 795; TUNEL, Roche, Mannheim, Germany) and the nuclei were counterstained with 4',6-diamino-2-phenylindole (D9542; DAPI, Sigma-Aldrich). Quantitative digital image analysis was performed from three randomly chosen representative areas selected from each slide using Image Pro 5.0 software (Media-Cybernetics, Rockville, MD, USA).

### ***Transcriptome microarray analysis***

Total RNA was isolated from the bladder tissues from AI-30 and sham groups using the RNeasy Mini Kit (QIAGEN, Valencia, CA, USA), including treatment with DNase I (QIAGEN). One microgram of total RNA was subjected to analysis using the Affymetrix GeneChip Rat Gene 2.0 ST Array (Affymetrix, Santa Clara, CA, USA). Microarray image data were processed on a GeneChip GCS3000 Scanner and Command Console software (Affymetrix). After importing CEL files of six samples (three independent samples from each group), the data were summarized and normalized using the robust multi-average

(RMA) method implemented in the Affymetrix Expression Console Software.

Functional analysis of transcriptomes was performed using KEGG pathway analysis (KEGG, <http://www.kegg.jp/kegg/pathway.html>) or Gene Set Enrichment Analysis (GSEA; Broad Institute, Cambridge, MA, USA) microarray software with default settings, as described previously<sup>57, 58</sup>. In the KEGG pathway analysis, 1.5-fold up- or down-regulation with  $p < 0.05$  was defined as the cut-off value for significant change. For GSEA analysis, gene sets were obtained from published literature or filtered from a curated functional gene set (C2) database. The transcriptome data discussed in this study have been deposited in the Gene Expression Omnibus of the NCBI and are accessible under GEO Series accession number GSE122060.

#### ***Real-time quantitative PCR (RQ-PCR) analysis***

Reverse transcription of the isolated total RNA was performed using TaqMan reverse transcription reagents (Applied Biosystems) and the expression level of the indicated transcripts was quantified by RQ-PCR with the PikoReal™ RT-PCR System (Thermo Scientific) with iQ™ SYBR Green PCR Master Mix (Bio-Rad, Hercules, CA), as described previously<sup>59, 60</sup>. Two randomly chosen areas from each slide or duplicated RQ-PCR assays (n=10) using five independent animals were used to quantify the digital image or gene expression data.

#### ***Statistics***

Data are reported as the mean  $\pm$  standard error of the mean (SEM) and were analyzed using GraphPad Prism 6.0 software (GraphPad Software, La Jolla, CA). Differences and significance were verified by one-way or two-way ANOVA followed by Bonferroni post hoc tests. A p-value  $< 0.05$  was considered as statistically significant.

## RESULTS

### *24-hour voiding pattern analysis in CBI model.*

To examine whether the severity of VED of bilateral iliac arteries could affect the bladder voiding functions, 10, 20, and 30 repetitions of AI, followed by a 1.25% high cholesterol diet for 8 weeks were applied to the rat model (**Fig. 2-1a**).

In the AI-10, AI-20, and AI-30 groups, the MV was less than in the sham group (all  $p < 0.01$ ; **Fig. 2-1b and 2-1c**). In the AI-10 group, the micturition interval (MI) tended to be shorter than that of the sham group but the difference was not statistically significant (**Fig. 2-1C**). In contrast, in the AI-20 and AI-30 groups, MI was significantly longer than in the sham group ( $p < 0.01$  and  $p < 0.001$ ). ). More importantly, in the AI-30 treated group, the number of voidings and total voiding volume were significantly decreased compared to those of the sham group ( $p < 0.01$  and  $p < 0.001$ ; **Fig. 2-1b and 2-1c**).

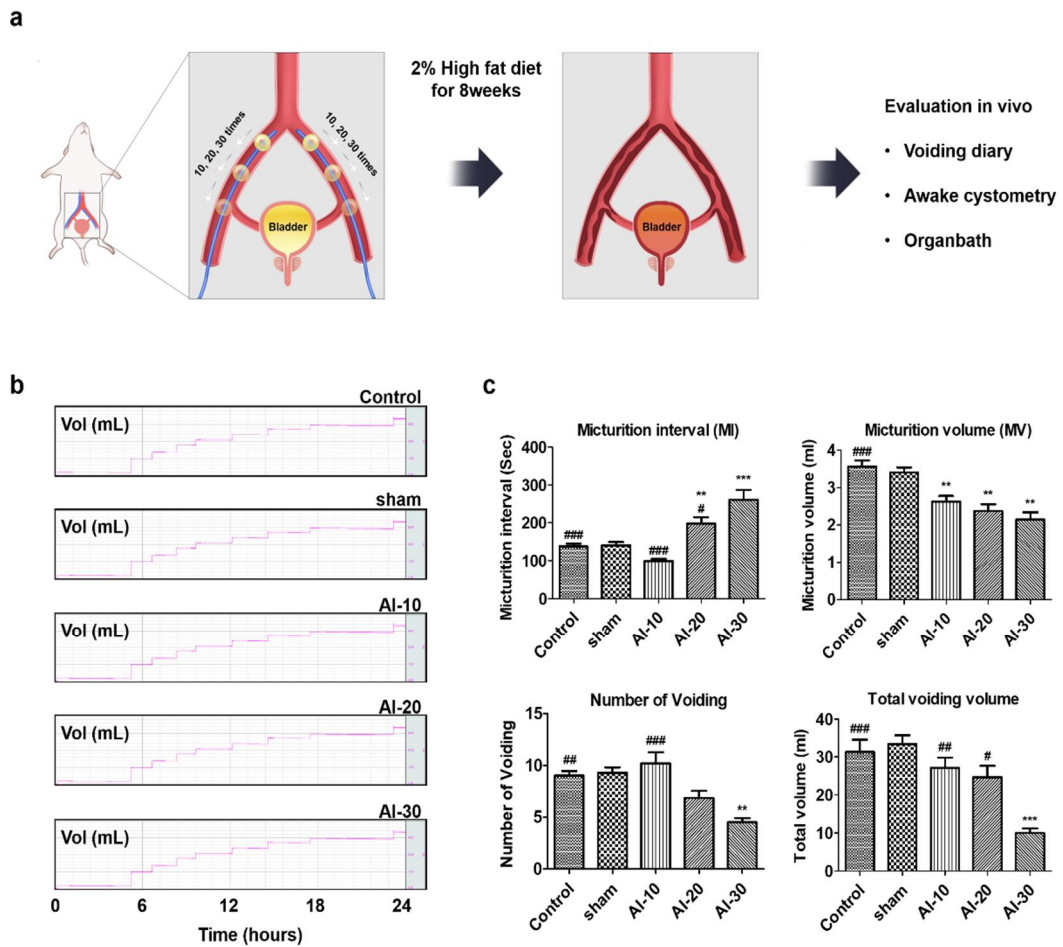


**Figure 2-1. CBI modeling schematic diagram and voiding diary for 24hours.**

(a) After induction of endothelial damage by balloon in iliac artery of rats fed high cholesterol diet for 8 weeks. (b) Representative 24 hours urine measurement results and (c) quantitative bladder voiding parameters at 8 week after iliac artery injury.

Control n= 12; sham n= 12; AI-10 n=10; AI-20 n=8; AI-30 n=8. All data are presented as the mean  $\pm$  SEM, \*p < 0.05, \*\*p < 0.01, \*\*\*p < 0.001 compared to the sham group; #p < 0.05, ##p < 0.01, ###p < 0.001 compared to the AI-30 group;

### *Measurement of bladder function in CBI model.*

Next performed awake filling and voiding cystometrograms studies, which allow long-term evaluation of bladder voiding function in free-moving animals<sup>77-79</sup>.

In line with the results of the 24-hour voiding pattern analysis, the changes in the dynamics of voiding function assessed by the awake cystometrograms were dramatically different according to the degree of vascular injury (**Fig. 2-2**). In the AI-10 group, voiding contractions were more frequently observed (**Fig. 2-2a**), and the MI was significantly shorter than that of sham group ( $p < 0.001$ ; **Fig. 2-2b**). However, maximum pressure and micturition pressure were not significantly reduced compared to the sham group. The MV of the AI-10 group was significantly smaller than that of the sham group ( $p < 0.05$ ), whereas the RV of the AI-10 group was not significantly increased (**Fig. 2-2b**).

Conversely, in the AI-20 and AI-30 groups, voiding contractions were less frequent (**Fig. 2-2a**), and the MI of the AI-20 and AI-30 groups was significantly longer than that of the sham group ( $p < 0.01$ ; **Fig. 2-2b**). Moreover, maximum pressure and micturition pressure of both AI-20 and AI-30 groups were also reduced compared to the sham group. In particular, in the AI-30 group, both the maximum and micturition pressures were significantly reduced ( $p < 0.001$  and  $p < 0.01$ ) and the RV was significantly increased compared to the sham group ( $p < 0.001$ ). Collectively, these results indicated that the degree of VED altered bladder functions ranging from DO to DUA and also suggested that progressive VED tended to induce DUA rather than DO (**Fig. 2-2b**).

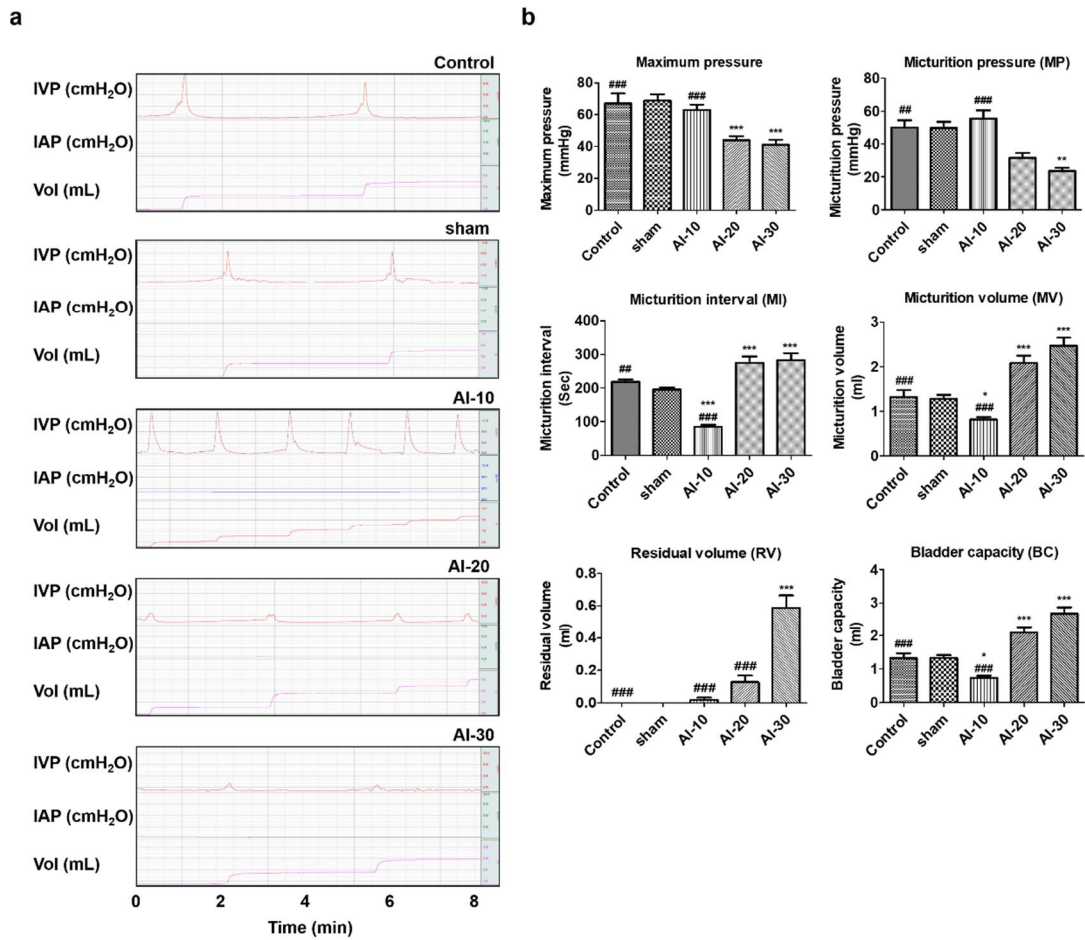


**Figure 2-2. Cystometrogram analysis.**

(a) Representative awake cystometry results and (b) quantitative bladder voiding data at 8 week after iliac artery injury rats. Control n= 12; sham n= 11; AI-10 n=13; AI-20 n=12; AI-30 n=10. All data are presented as the mean  $\pm$  SEM, \* $p < 0.05$ , \*\* $p < 0.01$ , \*\*\* $p < 0.001$  compared to the sham group; # $p < 0.05$ , ## $p < 0.01$ , ### $p < 0.001$  compared to the AI-30 group;

***Contractile changes induced by chronic ischemia induced.***

Thereafter, to assess changes in the overall contractile response, bladder strips of all groups were initially exposed to KCl (**Fig. 2-3a**). The mean contractile responses to KCl in the AI-10, AI-20, and AI-30 groups decreased according to the degree of vascular injury and were significantly lower than in the sham group (all  $p < 0.001$  **Fig. 2-3a**). Contractile responses induced by EFS were significantly reduced according to the degree of vascular injury at all frequencies (1Hz to 32Hz) (all  $p < 0.01$ ; **Fig. 2-3b**). The contractile responses to 1 mM ATP in the AI-10, AI-20 and AI-30 groups were significantly lower than in the sham group (all  $p < 0.001$ ) and were lower according to the degree of vascular injury (**Fig. 2-3c**). The response to carbachol in the AI-10, AI-20, and AI-30 groups at the concentrations of 1  $\mu$ M to 1 mM were significantly lower than in the sham group ( $p < 0.05$ ), and the reductions in response to carbachol were dependent on the degree of vascular injury (**Fig. 2-3d**).

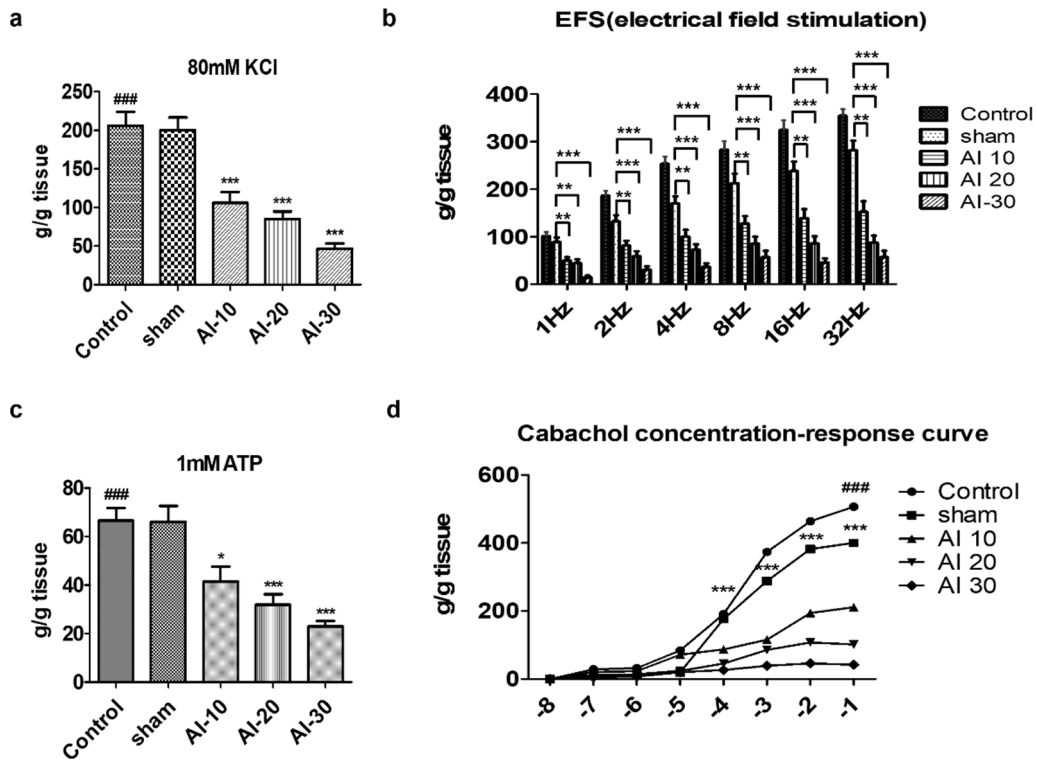


**Figure 2-3. Assessment of bladder smooth muscle contraction.**

(a) Contractile response to 80 mM KCl; (b) frequency–response to EFS (c) contractile response to 1 mM ATP; and (d) concentration–response curve to carbachol. Control n= 7 (14 bladder strip); sham n= 7 (14 bladder strip); AI-10 n=6 (12 bladder strip); AI-20 n=7 (14 bladder strip); AI-30 n=7 (14 bladder strip). All data are presented as the mean ± SEM, \*p < 0.05, \*\*p < 0.01, \*\*\*p < 0.001 compared to the sham group; #p < 0.05, ###p < 0.01, ####p < 0.001 compared to the AI-30 group;

### ***Histological evaluation of bladder tissue and common iliac arterial wall.***

Hematoxylin and eosin staining of iliac artery cross-sections from the AI groups demonstrated obvious arterial wall thickening (**Fig. 2-4a** and **2-4f**). In particular, the AI-30 group showed prominent neointimal formation compared to the sham and other AI groups (**Fig. 2-4a**). The average iliac artery wall thicknesses in the AI-10, AI-20, and AI-30 groups were significantly greater than in the sham group (all  $p < 0.001$ ) and showed a tendency for greater thickness with higher degree of vascular injury (**Fig. 2-4f**).

### ***Histo-pathophysiological analysis***

Compared to the sham group, the bladder tissues in the AI-10, AI-20, and AI-30 groups demonstrated significant increase in the infiltration of toluidine blue-stained mast cells (**Fig. 2-4b** and **2-4g**). Masson's trichrome staining of bladder tissue revealed an increased percent of collagen in the muscle layer in the AI-10, AI-20, and AI-30 groups compared to the sham group (**Fig. 2-4c**). The AI-10, AI-20, and AI-30 groups differed significantly from the sham-operated animals, respectively (**Fig. 2-4h**). Moreover, significant denervation in the bladder muscle layer of AI-10, AI-20, and AI-30 groups (all  $p < 0.001$ ) was observed on NE-100 staining (**Fig. 2-4d** and **2-4i**). In addition, immunostaining with anti-alpha smooth muscle actin antibody revealed that the bladder muscle layer in the AI-10 ( $p < 0.01$ ), AI-20 ( $p < 0.001$ ), and the AI-30 ( $p < 0.001$ ) groups was significantly more atrophic than in the sham group and the severity of this effect was dependent on the degree of vascular injury (**Fig. 2-4e** and **2-4j**).

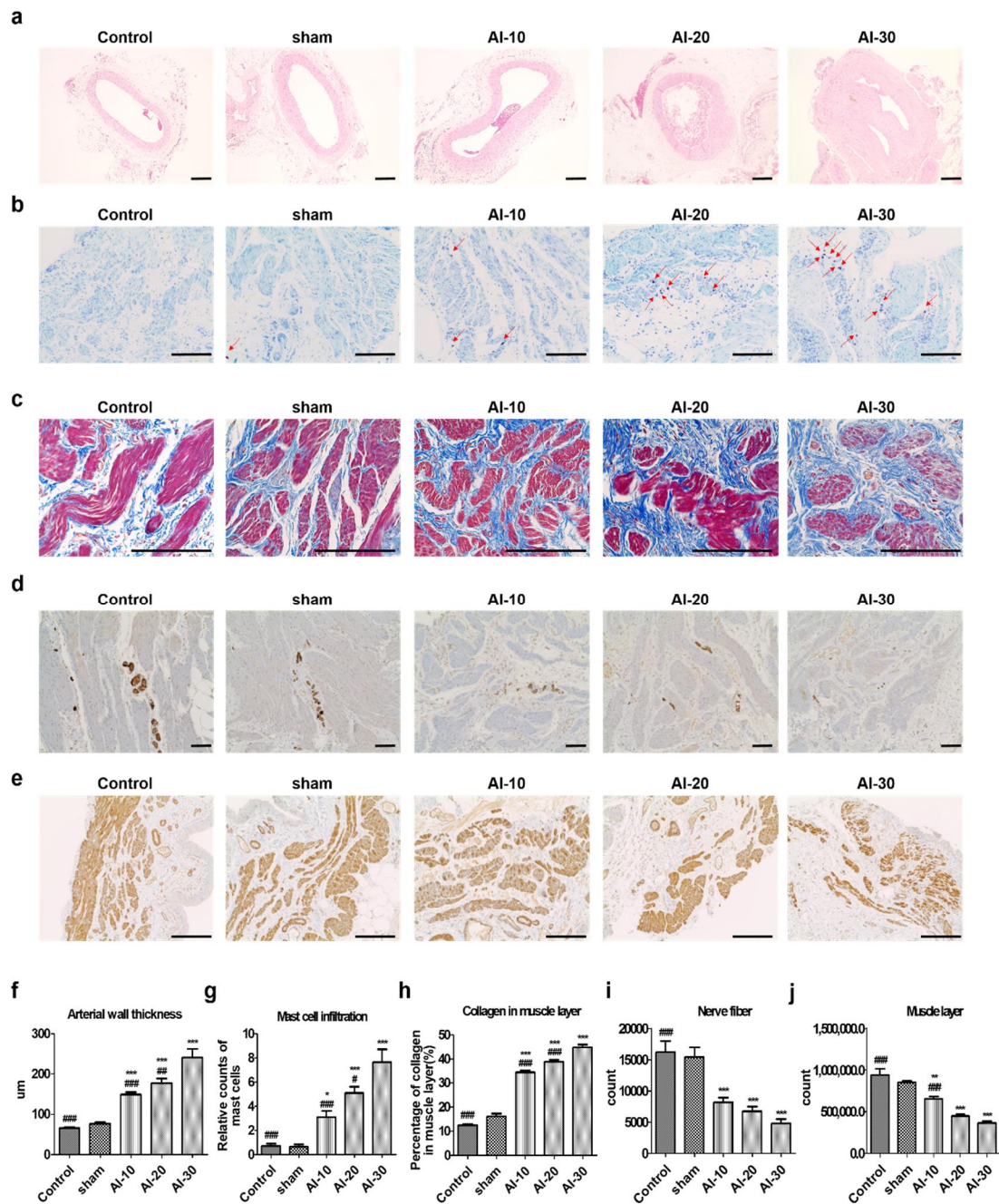


**Figure 2-4. Histologic examination.**

(a) Hematoxylin and eosin (H&E) staining in the iliac artery tissues (magnification  $\times 100$ , scale bar = 200  $\mu\text{m}$ ). (b) Toluidine blue staining (magnification  $\times 200$ , scale bar = 200  $\mu\text{m}$ ), and (c) Masson's trichrome staining (magnification  $\times 400$ , scale bar = 200  $\mu\text{m}$ ). (d) Neurofilament 200 (magnification  $\times 100$ , scale bar = 200  $\mu\text{m}$ ), and (e) alpha smooth muscle

actin (magnification  $\times 400$ , scale bar = 200  $\mu\text{m}$ ). (f, g, h, i, j) Histologic quantification after 8 weeks with iliac artery injury.

Control n= 10; sham n= 10; AI-10 n=10; AI-20 n=10; AI-30 n=10.

All data are presented as the mean  $\pm$  SEM, \*p < 0.05, \*\*p < 0.01, \*\*\*p < 0.001 compared to the sham group; #p < 0.05, ##p < 0.01, ###p < 0.001 compared to the AI-30 group;

*Apoptosis in endothelial cell and muscle cell.*

TUNEL staining of bladder tissues revealed a significantly higher percentage of apoptosis in the endothelium (**Fig. 2-5a and 2-5c**) and muscle layer (**Fig. 2-5b and 2-5d**) in the AI-20 and AI-30 groups compared with the sham group. The AI-10 group tended to have more frequent apoptosis in the mucosa and in muscle layer, but the difference failed to reach statistical significance (**Fig. 2-5**). Taken together, these histological examinations suggested that a high degree of atherosclerotic occlusion by progressive VED (AI-20 and AI-30 groups) induced histological features frequently observed in the bladder of patients with DUA including tissue inflammation, fibrosis, denervation, muscular degeneration, and increased apoptosis of the bladder muscle tissue.

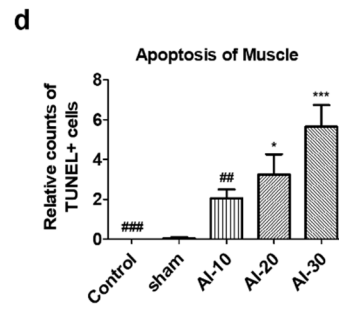
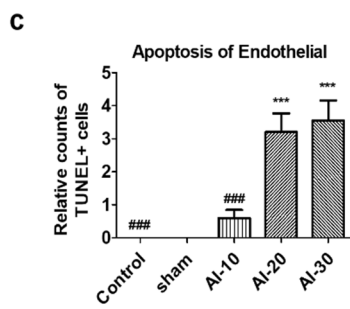
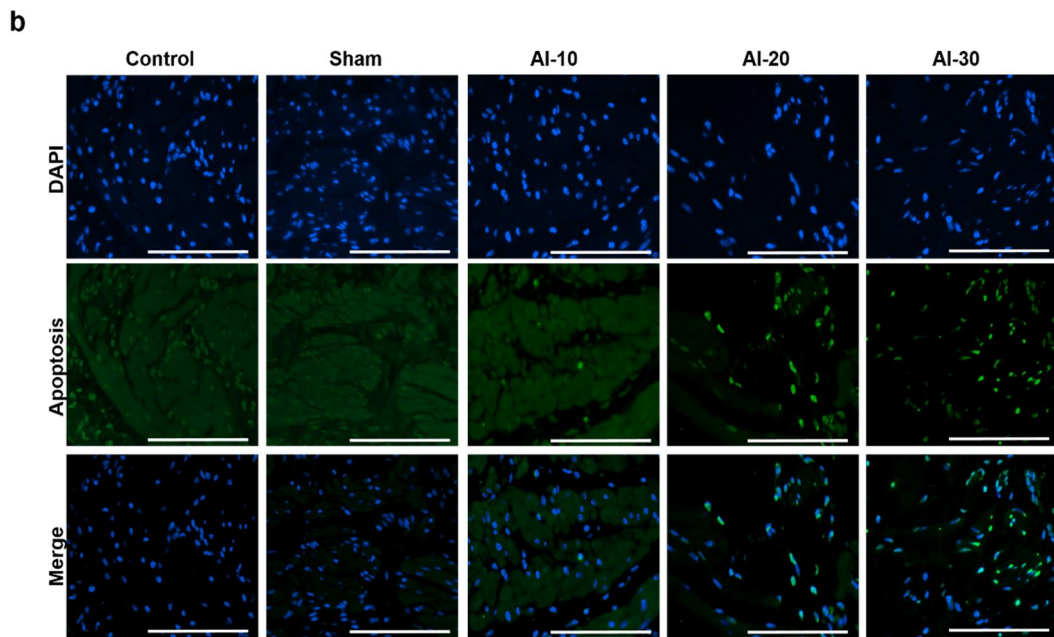
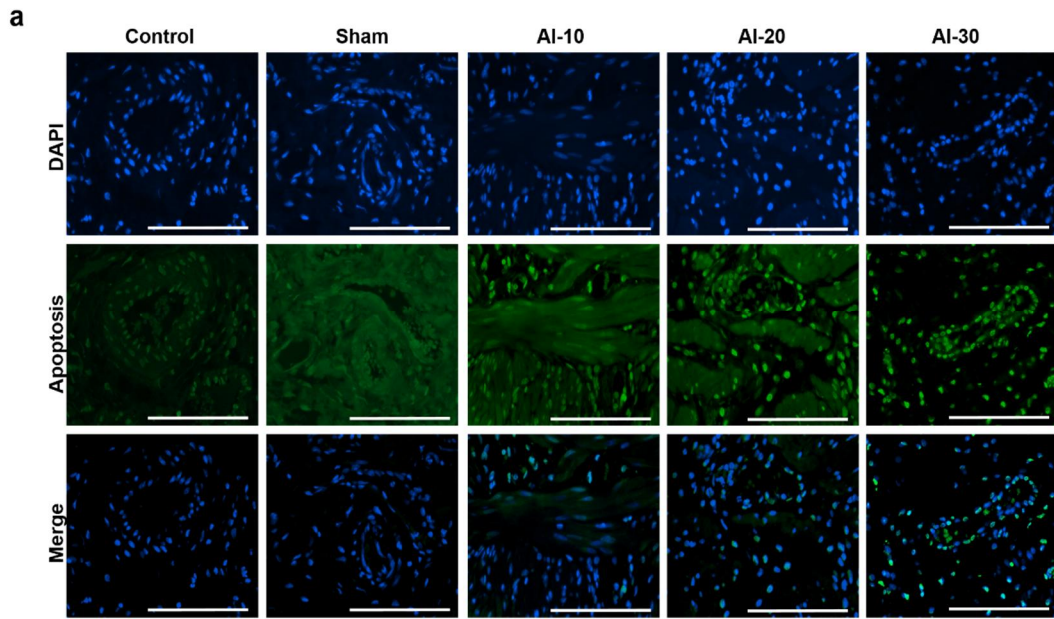


**Figure 2-5. Immunofluorescent analysis.**

(a, b) TUNEL assay (magnification  $\times 400$ , scale bar = 200  $\mu\text{m}$ ) and (c, d) histologic quantification after 8 weeks with iliac artery injury.

Control n= 10; sham n= 10; AI-10 n=10; AI-20 n=10; AI-30 n=10. All data are presented as the mean  $\pm$  SEM, \*p < 0.05, \*\*p < 0.01, \*\*\*p < 0.001 compared to the sham group; #p < 0.05, ##p < 0.01, ###p < 0.001 compared to the AI-30 group;

### ***Gene expression study***

To obtain molecular insight into DUA induced by ischemic vascular injury, this study compared the genome-wide gene expression profiles of bladder tissues of sham and AI-30-treated groups. Based on cut-off values with a fold change of more than 1.5 and p-value <0.05, approximately 170 genes were differentially expressed genes (DEGs) and the majority (139 genes) were up-regulated in the AI-30 group (**Fig. 2-6a and 2-6b**). KEGG pathway analysis indicated that DEGs between AI-30 and the sham groups were significantly associated with interleukin-17 (IL-17) and hypoxia inducible factor-1 (HIF-1) pathways (**Fig. 2-6C**). In particular, the up-regulation of NFKB Inhibitor-alpha (*Nfkbia*), C-X-C motif chemokine ligand-2 (*Cxcl2*), and S100 calcium binding protein-A9 (*S100a9*) was significant in the IL-17 pathway (**Fig. 2-6D**) and interferon gamma receptor-1 (*Ifngr1*), transferrin (*Tf*), and vascular endothelial growth factor-A (*Vegfa*) were considered key contributing genes for the significant differences observed in HIF pathways following AI-30 injury (**Fig. 2-6b and 2-6C**). RQ-PCR analysis validated that AI-30 injury specifically increased the transcription of the aforementioned genes associated with the IL-17 (**Fig. 2-6E**) and HIF-1 (**Fig. 2-6F**) pathways. In addition, this study identified an additional 25 genes belonging to distinct biological pathways altered in the response to AI-30 injury (**Table 1**). These include phospholipase A2 group IIA (*Pla2g2a*) and colony stimulating factor-3 receptor (*Csf3r*), involved in ether lipid metabolism or cytokine-cytokine receptor interaction pathways, respectively. In addition, progressive AED injury significantly increased the transcription of complement factor-H (*Cfh*), C2 complement (*C2*), Fc fragment of immunoglobulin G receptor-IIb (*Fcgr2b*), and interferon-induced protein with tetratricopeptide repeats 1B-like (*Ifit1bl*), genes related to pathogen infection processes (**Fig. 2-6f**).

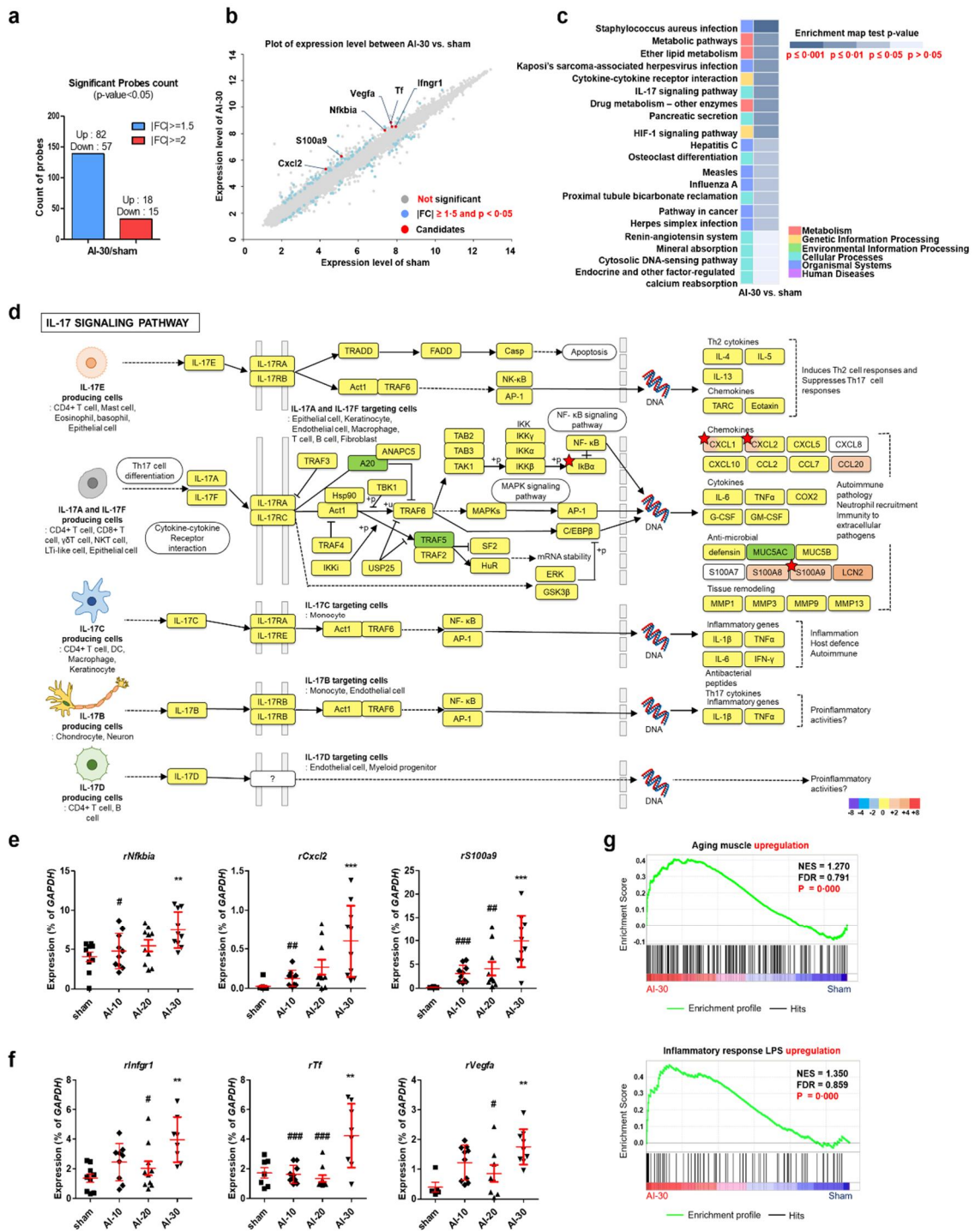


**Figure 2-6. Gene analysis.**

Control n= 10; sham n= 10; AI-10 n=10; AI-20 n=10; AI-30 n=10. All data are presented as the mean  $\pm$  SEM, \* $p < 0.05$ , \*\* $p < 0.01$ , \*\*\* $p < 0.001$  compared to the sham group; # $p < 0.05$ , ## $p < 0.01$ , ### $p < 0.001$  compared to the AI-30 group;

## DISCUSSION

In the present study identified that progressive VED of bilateral iliac arteries, without the contribution of any of enhancers, successfully induced changes in bladder function similar to DUA in a rat model. These findings suggest that CBI may be responsible for a major pathogenetic mechanism observed in DUA. The understanding of the pathogenesis of DUA remains uncertain. However, it is likely to be multifactorial<sup>65</sup>. It is recognized that detrusor contractility diminishes with aging although not all individuals develop clinically relevant DUA<sup>57</sup>. It is presumed that multifactorial conditions may cause DUA. In some patients without any pathological causes, an age-related decrease in detrusor contractility might be primarily responsible for “idiopathic” DUA and this might explain why the gene set related to aging muscle was characteristically enriched by progressive VED (**Fig. 2-6F**). In other patients, relevant conditions such as diabetes mellitus, neural injury, or bladder outlet obstruction may lead to “secondary” DUA<sup>76</sup>.

Using previously-established rat models, it has been suggested that CBI induced by VED combined with a high-cholesterol diet can lead to functional and structural changes in the bladder<sup>69-71</sup>. However, as mentioned above, changes observed in voiding patterns induced in previous CBI rat models have also been varied<sup>70,71,81</sup>. Nomiya et al. first reported that balloon endothelial injury of the iliac arteries (performed 10 times on each side) with 8 weeks of a high cholesterol diet induced DO manifested as an increase in voiding frequency<sup>71</sup>, and proposed that oxidative stress and inflammation may be key factors in the development of DO<sup>81</sup>. Conversely, the same study group also reported that the CBI rat model produced fibrosis and a reduction in the number of nerves innervating the bladder, which led to decreased bladder contractility in the same setting (10 times of both iliac arterial injury combined with a high cholesterol diet)<sup>70</sup>.

The results of our study also demonstrated a wide spectrum of changes in the bladder

function according to the degree of VED. In the AI-10 group, voiding contractions were more frequently observed (**Fig. 2-2a**) and the MI was significantly shorter than that of the sham group (**Fig. 2-2b**). These results were similar to those of the former study by Nomiya et al<sup>71</sup>, which reproduced the DO.

Conversely, more progressive vascular damage resulted in different results. In the AI-20 and AI-30 groups, voiding contractions tended to be less frequent (**Fig. 2-2a**), and the MI of AI-20 and AI-30 group were significantly longer than that of the sham group (**Fig. 2-2b**). In particular, in the AI-30 group, micturition pressure was significantly reduced and RV was significantly increased compared to the sham group (**Fig. 2-2b**). Moreover, our results from organ bath studies confirmed that contractile responses to various stimulations decreased proportionately with the degree of vascular injury (**Fig. 2-3**). These results implied that some degree of bladder ischemia induced by VED could result in the development of DO manifested as an increase in voiding frequency, however, more progressive VED and ischemia may reduce the bladder contractility and therefore result in DUA manifested as an emptying failure.

These findings are in agreement with a more recent study by Nomiya et al.<sup>69</sup>, which also reported that progressive VED induced DUA in a rat model. In that study, rats were exposed to L-NAME (3 mg/mL dissolved in drinking water) to enhance the morphological vascular intimal changes, in addition to the VED (10 times to both iliac arteries) and a high cholesterol diet. The iliac arteries of the injury/L-NAME groups showed more prominent neointimal formation and luminal occlusion. Furthermore, the RV in the injury/L-NAME group tended to be increased, while bladder contractility was significantly decreased compared to those in controls<sup>69</sup>. Although, the negative effects of L-NAME on blood flow via the vascular intimal change have been demonstrated in previous rat model studies<sup>69, 82, 83</sup>, L-NAME, may also exaggerate the effects of hypoxic damage via generation of nitrogen species<sup>84</sup>. Therefore, chronic exposure to L-NAME may have a direct effect on bladder

function in rat models<sup>85</sup>.

For these reasons, study simply hypothesized that sufficient physical damage for VED itself is enough to induce DUA. Our results clearly showed that sufficient VED (AI-30) successfully caused prominent arterial wall thickening and neointimal formation compared with the sham-operated and other AI groups (**Fig. 2-4a**). Moreover, our AI-30 group without any exposure to the artificial enhancer drug, reproduced similar changes in bladder functions as DUA, as observed in the injury/L-NAME groups of a previous study<sup>69</sup>. In particular, in the previous model by Nomiya et al., the injury/L-NAME group did not demonstrated any significant decrease in micturition pressure on cystometry assessment<sup>69</sup>, our result in the AI-30 group showed that maximum and micturition pressure were significantly reduced compared to the sham group (**Fig. 2-2b**). Therefore, study suggest that adequate VED alone is sufficient and more efficient for inducing the DUA in the rat model.

The pathophysiology of CBI-induced DUA has not been fully elucidated by previous studies<sup>69, 70</sup>. These studies have suggested that collagen deposition in the muscle layer<sup>69, 70</sup> and significantly fewer nerves in the bladder wall<sup>70</sup> caused by oxidative stress from chronic bladder ischemia may be the possible causes for decreased contractile function based on histological evaluations. However, these previous studies did not consistently report the results of histological changes of the CBI-induced DUA rat model<sup>69, 70</sup>. This results clearly showed that progressive VED induced mast cell infiltration (**Fig. 2-4b** and **2-4g**) and collagen deposition in the muscle layer (**Fig. 2-4c** and **2-4h**). Moreover, significantly fewer nerves in the bladder wall of AI-10, AI-20, and AI-30 groups were also observed (**Fig. 2-4d** and **2-4i**). These results are in agreement with previous studies<sup>69, 70</sup>. In addition, this study also observed a significant atrophy of the bladder detrusor muscle in the AI groups (**Fig. 2-4e** and **2-4j**). Our results based on immunofluorescence staining suggest that this significant muscle atrophy is directly caused by the apoptosis of bladder muscle cells (**Fig. 2-5**). These results imply that oxidative stress from progressive chronic bladder ischemia causes the

inflammation of bladder tissue, and therefore it induces fibrosis and denervation of the bladder muscle layer, moreover it also induces apoptosis of bladder muscle tissues. In this regard, the transcriptome of bladder tissue of the AI-30 group was characteristically enriched by gene sets associated with oxidative stress and inflammatory responses (Supplementary Fig. 2). Thus, further study is required to identify a driver gene(s) responsible for these histological changes and to advance our understanding of the pathogenesis of impaired detrusor contractility induced by the progressive VED.

Regarding the possible pathophysiology of DUA induced by progressive VED at the genetic level little is known. Some researchers have proposed the transforming growth factor- $\beta$ 1 (TGF- $\beta$ 1) pathway as a possible pathophysiological mechanism for DUA<sup>70</sup>. However, this suggestion was supported by the results from another researcher group, which demonstrated that the expression of TGF- $\beta$ 1 RNA and protein levels were increased in bladder tissue and that collagen fibers in the bladder muscle layer were increased in the rabbit CBI model<sup>78</sup>. Genome-wide gene expression analysis showed that genes (e.g. *Nfkbia*, *Cxcl2*, and *S100a9*) related to the IL-17 and HIF pathways (Fig. 2-6d and 2-6e) were particularly upregulated by progressive VED. In several chronic tissue injuries models including bleomycin-treated mice, the production of T cell IL-17 is a key mediator of tissue inflammation and subsequent fibrosis through the activation of TGF- $\beta$  signaling<sup>83</sup>. Furthermore, the abnormal expression of *Nfkbia*, *Cxcl2*, and *S100a9* has been associated with the pathogenesis of a wide range of chronic inflammation and age-related tissue degeneration disorders<sup>84-85</sup>. Therefore, as a future study will attempt not only to identify the crucial gene(s) involved in DUA pathogenesis, but also to develop an associated novel therapeutic strategy for treating these intractable bladder voiding dysfunction disorders.

## CONCLUSIONS

In the present study, A rat model of progressive VED without any the use of artificial enhancers successfully induced DUA. Our data suggest that oxidative stress from progressive VED followed by tissue inflammation, fibrosis, denervation, and apoptosis of the bladder muscle tissue may represent underlying mechanisms for CBI-induced DUA. At the genetic level, IL-17 and HIF-1 signaling pathways including INF- $\gamma$  receptor-1 and *Cxcl2* seem to be the key modes of action, which provoke DUA, and might represent helpful treatment targets for DUA in the future.

## REFERENCE

1. Offiah, I. *et al.* The Expression of Inflammatory Mediators in Bladder Pain Syndrome. *European Urology* **70**, 283-290 (2016).
2. Propert, K. J. *et al.* A prospective study of interstitial cystitis: results of longitudinal followup of the interstitial cystitis data base cohort. The Interstitial Cystitis Data Base Study Group. *J Urol* **163**, 1434-1439 (2000).
3. Tripp, D. A. *et al.* Mapping of Pain Phenotypes in Female Patients with Bladder Pain Syndrome/Interstitial Cystitis and Controls. *European Urology* **62**, 1188-1194 (2012).
4. Kim, H.-J. Update on the Pathology and Diagnosis of Interstitial Cystitis/Bladder Pain Syndrome: A Review. *Int Neurourol J* **20**, 13-17 (2016).
5. Clemens, J. Q. *et al.* Prevalence of painful bladder symptoms and effect on quality of life in black, Hispanic and white men and women. *J Urol* **177**, 1390-1394 (2007).
6. van Ophoven, A., Pokupic, S., Heinecke, A. & Hertle, L. A prospective, randomized, placebo controlled, double-blind study of amitriptyline for the treatment of interstitial cystitis. *J Urol* **172**, 533-536 (2004).
7. Nickel, J. C. *et al.* Pentosan polysulfate sodium for treatment of interstitial cystitis/bladder pain syndrome: insights from a randomized, double-blind, placebo controlled study. *J Urol* **193**, 857-862 (2015).
8. Hanno, P. M., Erickson, D., Moldwin, R., Faraday, M. M. & American Urological, A. Diagnosis and treatment of interstitial cystitis/bladder pain syndrome: AUA guideline amendment. *J Urol* **193**, 1545-1553 (2015).
9. Sairanen, J. *et al.* Cyclosporine A and pentosan polysulfate sodium for the treatment of interstitial cystitis: a randomized comparative study. *J Urol* **174**, 2235-2238 (2005).
10. Evans, R. J. *et al.* Proof of concept trial of tanezumab for the treatment of symptoms associated with interstitial cystitis. *J Urol* **185**, 1716-1721 (2011).
11. Ryu, J. *et al.* Elimination of Hunner's Ulcers by Fulguration in Patients With Interstitial Cystitis: Is It Effective and Long Lasting? *Korean journal of urology* **54**,

- 767-771 (2013).
12. Kim, A., Shin, D.-M. & Choo, M.-S. Stem Cell Therapy for Interstitial Cystitis/Bladder Pain Syndrome. *Current Urology Reports* **17**, 1-9 (2015).
  13. Song, M. *et al.* Mesenchymal Stem Cell Therapy Alleviates Interstitial Cystitis by Activating Wnt Signaling Pathway. *Stem Cells and Development* **24**, 1648-1657 (2015).
  14. Kim, A. *et al.* Mesenchymal stem cells protect against the tissue fibrosis of ketamine-induced cystitis in rat bladder. *Scientific Reports* **6**, 30881 (2016).
  15. Kim, H.-S. *et al.* Clinical Trial of Human Umbilical Cord Blood-Derived Stem Cells for the Treatment of Moderate-to-Severe Atopic Dermatitis: Phase I/IIa Studies. *STEM CELLS* **35**, 248-255 (2017).
  16. Zhu, H. *et al.* Therapeutic Effects of Human Umbilical Cord-Derived Mesenchymal Stem Cells in Acute Lung Injury Mice. *Scientific Reports* **7**, 39889 (2017).
  17. He, Z. *et al.* Intravenous hMSCs Ameliorate Acute Pancreatitis in Mice via Secretion of Tumor Necrosis Factor- $\alpha$  Stimulated Gene/Protein 6. *Scientific Reports* **6**, 38438 (2016).
  18. Tebebi, P. A. *et al.* Improving the therapeutic efficacy of mesenchymal stromal cells to restore perfusion in critical limb ischemia through pulsed focused ultrasound. *Scientific Reports* **7**, 41550 (2017).
  19. Kyu-Hyun, H., Ae-Kyeong, K. & and Dong-ik, K. Therapeutic Potential of Human Mesenchymal Stem Cells for Treating Ischemic Limb Diseases. *International Journal of Stem Cells* **9**, 163-168 (2016).
  20. Thomson, J. A. *et al.* Embryonic Stem Cell Lines Derived from Human Blastocysts. *Science* **282**, 1145-1147 (1998).
  21. Evans, M. J. & Kaufman, M. H. Establishment in culture of pluripotential cells from mouse embryos. *Nature* **292**, 154-156 (1981).
  22. Fandel, T. M. *et al.* Transplanted Human Stem Cell-Derived Interneuron Precursors Mitigate Mouse Bladder Dysfunction and Central Neuropathic Pain after Spinal Cord Injury. *Cell Stem Cell* **19**, 544-557 (2016).
  23. Kim, J. M. *et al.* Perivascular Progenitor Cells Derived From Human Embryonic

- Stem Cells Exhibit Functional Characteristics of Pericytes and Improve the Retinal Vasculature in a Rodent Model of Diabetic Retinopathy. *Stem Cells Transl Med* **5**, 1268-1276 (2016).
24. Hong, K.-S. *et al.* A Porous Membrane-Mediated Isolation of Mesenchymal Stem Cells from Human Embryonic Stem Cells. *Tissue Engineering Part C: Methods* **21**, 322-329 (2014).
  25. Shie, J. H. & Kuo, H. C. Higher levels of cell apoptosis and abnormal E-cadherin expression in the urothelium are associated with inflammation in patients with interstitial cystitis/painful bladder syndrome. *BJU Int* **108**, E136-141 (2011).
  26. Logadottir, Y. *et al.* Cytokine expression in patients with bladder pain syndrome/interstitial cystitis ESSIC type 3C. *J Urol* **192**, 1564-1568 (2014).
  27. Sant, G. R., Kempuraj, D., Marchand, J. E. & Theoharides, T. C. The mast cell in interstitial cystitis: role in pathophysiology and pathogenesis. *Urology* **69**, 34-40 (2007).
  28. Liu, H. T. *et al.* Alteration of Urothelial Inflammation, Apoptosis, and Junction Protein in Patients with Various Bladder Conditions and Storage Bladder Symptoms Suggest Common Pathway Involved in Underlying Pathophysiology. *Lower urinary tract symptoms* **7**, 102-107 (2015).
  29. Ustinova, E. E., Fraser, M. O. & Pezzone, M. A. Colonic irritation in the rat sensitizes urinary bladder afferents to mechanical and chemical stimuli: an afferent origin of pelvic organ cross-sensitization. *Am J Physiol Renal Physiol* **290**, F1478-1487 (2006).
  30. Nickel, J. C. *et al.* Interstitial cystitis/painful bladder syndrome and associated medical conditions with an emphasis on irritable bowel syndrome, fibromyalgia and chronic fatigue syndrome. *J Urol* **184**, 1358-1363 (2010).
  31. Malykhina, A. P. *et al.* Hyperexcitability of convergent colon and bladder dorsal root ganglion neurons after colonic inflammation: mechanism for pelvic organ cross-talk. *Neurogastroenterol Motil* **18**, 936-948 (2006).
  32. Dihlmann, S., Siermann, A. & von Knebel Doeberitz, M. The nonsteroidal anti-inflammatory drugs aspirin and indomethacin attenuate beta-catenin/TCF-4

- signaling. *Oncogene* **20**, 645-653 (2001).
33. van der Poel, H. G. Smart Drugs in Prostate Cancer. *European Urology* **45**, 1-17.
  34. Saito, K. *et al.* Luminescent proteins for high-speed single-cell and whole-body imaging. *Nat Commun* **3**, 1262 (2012).
  35. Golubeva, A. V., Zhdanov, A. V., Mallel, G., Dinan, T. G. & Cryan, J. F. The mouse cyclophosphamide model of bladder pain syndrome: tissue characterization, immune profiling, and relationship to metabotropic glutamate receptors. *Physiological reports* **2**, e00260 (2014).
  36. Kim, J. K. *et al.* Fabrication and operation of GRIN probes for in vivo fluorescence cellular imaging of internal organs in small animals. *Nat. Protocols* **7**, 1456-1469 (2012).
  37. Chancellor, M. B. & Yoshimura, N. Treatment of interstitial cystitis. *Urology* **63**, 85-92 (2004).
  38. Mullins, C., Bavendam, T., Kirkali, Z. & Kusek, J. W. Novel research approaches for interstitial cystitis/bladder pain syndrome: thinking beyond the bladder. *Translational andrology and urology* **4**, 524-533 (2015).
  39. Belknap, S., Blalock, E. & Erickson, D. The Challenges of Interstitial Cystitis: Current Status and Future Prospects. *Drugs* **75**, 2057-2063 (2015).
  40. Maeda, D. *et al.* Hunner-Type (Classic) Interstitial Cystitis: A Distinct Inflammatory Disorder Characterized by Pancystitis, with Frequent Expansion of Clonal B-Cells and Epithelial Denudation. *PLoS One* **10**, e0143316 (2015).
  41. Malykhina, A. P. Neural mechanisms of pelvic organ cross-sensitization. *Neuroscience* **149**, 660-672 (2007).
  42. Vaquero, J., Zurita, M., Oya, S. & Santos, M. Cell therapy using bone marrow stromal cells in chronic paraplegic rats: Systemic or local administration? *Neuroscience Letters* **398**, 129-134 (2006).
  43. Lee, R. H. *et al.* Intravenous hMSCs Improve Myocardial Infarction in Mice because Cells Embolized in Lung Are Activated to Secrete the Anti-inflammatory Protein TSG-6. *Cell Stem Cell* **5**, 54-63 (2009).
  44. Schwartz, S. D. *et al.* Human embryonic stem cell-derived retinal pigment

- epithelium in patients with age-related macular degeneration and Stargardt's macular dystrophy: follow-up of two open-label phase 1/2 studies. *Lancet* **385**, 509-516 (2015).
45. Schwartz, S. D. *et al.* Embryonic stem cell trials for macular degeneration: a preliminary report. *Lancet* **379**, 713-720 (2012).
  46. de Almeida, P. E., Ransohoff, J. D., Nahid, A. & Wu, J. C. Immunogenicity of Pluripotent Stem Cells and Their Derivatives. *Circulation Research* **112**, 549-561 (2013).
  47. Drukker, M. *et al.* Human Embryonic Stem Cells and Their Differentiated Derivatives Are Less Susceptible to Immune Rejection Than Adult Cells. *STEM CELLS* **24**, 221-229 (2006).
  48. Kang, H. *et al.* The Therapeutic Effects of Human Mesenchymal Stem Cells Primed with Sphingosine-1 Phosphate on Pulmonary Artery Hypertension. *Stem Cells and Development* **24**, 1658-1671 (2015).
  49. Lim, J. *et al.* Priming with ceramide-1 phosphate promotes the therapeutic effect of mesenchymal stem/stromal cells on pulmonary artery hypertension. *Biochemical and Biophysical Research Communications* **473**, 35-41 (2016).
  50. Jin, H. J. *et al.* Senescence-Associated MCP-1 Secretion Is Dependent on a Decline in BMI1 in Human Mesenchymal Stromal Cells. *Antioxid Redox Signal* **24**, 471-485 (2016).
  51. Kumamaru, H. *et al.* Direct isolation and RNA-seq reveal environment-dependent properties of engrafted neural stem/progenitor cells. *Nat Commun* **3**, 1140 (2012).
  52. Zhang, C., Murphy, S. V. & Atala, A. Regenerative medicine in urology. *Seminars in pediatric surgery* **23**, 106-111 (2014).
  53. Sadri-Ardekani, H. & Atala, A. Regenerative medicine for the treatment of reproductive system disorders: current and potential options. *Advanced drug delivery reviews* **82-83**, 145-152 (2015).
  54. Song, M. *et al.* The Paracrine Effects of Mesenchymal Stem Cells Stimulate the Regeneration Capacity of Endogenous Stem Cells in the Repair of a Bladder-Outlet-Obstruction-Induced Overactive Bladder. *Stem Cells and Development* **23**, 654-663

- (2013).
55. Lee, T. & Yoon, S. M. The Role of Intra-abdominal Pressure Measurement in Awake Rat Cystometry. *Int Neurourol J* **17**, 44-47 (2013).
  56. Jin, L. H. *et al.* Urodynamic findings in an awake chemical cystitis rat model observed by simultaneous registrations of intravesical and intraabdominal pressures. *Int Neurourol J* **14**, 54-60 (2010).
  57. Heo, J. *et al.* Sirt1 Regulates DNA Methylation and Differentiation Potential of Embryonic Stem Cells by Antagonizing Dnmt3l. *Cell Rep* **18**, 1930-1945 (2017).
  58. Abrams P. *et al.* The standardisation of terminology of lower urinary tract function: report from the Standardisation Sub-committee of the International Continence Society. *Neurourol Urodyn* **21**, 167-78 (2002).
  59. Smith PP. Aging and the underactive detrusor: a failure of activity or activation?: *Neurourol Urodyn* **29**, 408-12 (2010).
  60. Andersson K-E. Detrusor underactivity/underactive bladder: new research initiatives needed. *J Urol* **184**, 1829-30 (2010).
  61. Madjar S, Appell RA. Impaired detrusor contractility: Anything new? *Curr Urol Rep* **3**, 373-7(2002).
  62. Gakis G. *et al.* Functional Detrusor Myoplasty for Bladder Acontractility: Long-Term Results. *J Urol* **185**, 593-9(2011).
  63. Kuhn W. *et al.* Intermittent urethral self-catheterisation: long term results (bacteriological evolution, continence, acceptance, complications). *Spinal Cord* **29**:222(1991).
  64. Manack A. *et al.* Epidemiology and healthcare utilization of neurogenic bladder patients in a US claims database. *Neurourol Urodyn* **30**, 395-401(2011).
  65. Jeong SJ. *et al.* Prevalence and Clinical Features of Detrusor Underactivity among Elderly with Lower Urinary Tract Symptoms: A Comparison between Men and Women. *Korean J Urol* **53**, 342-8(2012).
  66. Herrera MD. *et al.* Endothelial dysfunction and aging: an update. *AGEING RES REV* **9**, 142-52(2010).
  67. Azadzi KM. *et al.* Overactivity and structural changes in the chronically ischemic

- bladder. *J Urol* **162**, 1768-78(1999).
68. Azadzoï KM. *et al.* Atherosclerosis-induced chronic ischemia causes bladder fibrosis and non-compliance in the rabbit. *J Urol* **161**, 1626-35(1999).
  69. Nomiya M. *et al.* Progressive vascular damage may lead to bladder underactivity in rats. *J Urol* **191**, 1462-9(2014).
  70. Sagawa K. *et al.* Impaired Detrusor Contractility in a Rat Model of Chronic Bladder Ischemia. *Urology* **81**, 1379.e9-.e14 (2013).
  71. Nomiya M. *et al.* The effect of atherosclerosis-induced chronic bladder ischemia on bladder function in the rat. *Neurourol Urodyn* **31**, 195-200(2012).
  72. Lee T. *et al.* The Role of Intra-abdominal Pressure Measurement in Awake Rat Cystometry. *Int Neurourol J* **17**, 44-7(2013).
  73. Jin LH. *et al.* Urodynamic findings in an awake chemical cystitis rat model observed by simultaneous registrations of intravesical and intraabdominal pressures. *Int Neurourol J* **14**, 54-60(2010).
  74. Jin JH. *et al.* Senescence associated MCP-1 secretion is dependent on a decline in BMI1 in human mesenchymal stromal cells. *Antioxid Redox Signal* **24**, 471-85(2015).
  75. Jeong EM. *et al.* Real-Time Monitoring of Glutathione in Living Cells Reveals that High Glutathione Levels Are Required to Maintain Stem Cell Function. *Stem Cell Reports* **10**, 600-614(2018).
  76. Van Koeveringe G. *et al.* Detrusor underactivity: a plea for new approaches to a common bladder dysfunction. *Neurourol Urodyn* **30**, 723-8(2011).
  77. Kim A. *et al.* Improved efficacy and in vivo cellular properties of human embryonic stem cell derivative in a preclinical model of bladder pain syndrome. *Sci Rep* **7**,8872(2017).
  78. Lee SW. *et al.* The therapeutic effect of human embryonic stem cell-derived multipotent mesenchymal stem cells on chemical-induced cystitis in rats. *Int Neurourol J* **22**, S34-45(2018).
  79. Ryu C. *et al.* Longitudinal intravital imaging of transplanted mesenchymal stem cells elucidates their functional integration and therapeutic potency in an animal model of

- interstitial cystitis/bladder pain syndrome. *Theranostics* **8**, 5610-24(2018).
80. Nomiya M. *et al.* Increased bladder activity is associated with elevated oxidative stress markers and proinflammatory cytokines in a rat model of atherosclerosis-induced chronic bladder ischemia. *Neurourol Urodyn* **31**, 185-9(2012).
  81. Baylis C. *et al.* Chronic blockade of nitric oxide synthesis in the rat produces systemic hypertension and glomerular damage. *J Clin Invest* **90**, 278-81(1992).
  82. Son H, Lee SL. *et al.* New unstable bladder model in hypercholesterolemia rats. *Urology* **69**, 186-90(2007).
  83. Lin W-Y. *et al.* Effects of L-arginine and L-NAME on chronic partial bladder outlet obstruction in rabbit. *Am J Physiol Regul Integr Comp Physiol* **293**, R2390-R9(2007).
  84. Mónica FZ. *et al.* Long-term administration of BAY 41-2272 prevents bladder dysfunction in nitric oxide-deficient rats. *Neurourol Urodyn* **30**, 456-60(2011).
  85. Azadzoï KM. *et al.* Molecular reactions and ultrastructural damage in the chronically ischemic bladder. *J Urol* **186**, 2115-22(2011).

## 국문 초록

### 제 1 장.

방광통증 증후군의 전임상 모델에서 인간배아 줄기세포 유도체의 생체 내 특성 조사 및 치료효과와 효능 연구.

간질성방광염/방광통증 증후군(IC/BPS)는 극심한 골반통증과 빈뇨를 동반하는 난치성 질환이다. IC/BPS는 Hunner 궤양과 같은 특징적인 방광경 소견을 보이며, 심각한 요로상피의 결손과 방광의 염증 반응이 특징이다. 아직까지 질환의 기전이 명확하지 않으므로, 확실한 치료법 또한 없는 실정이다.

이러한 IC/BPS 질환을 치료하기 위한 간엽줄기세포(MSC)는 새로운 치료법으로 제시 되고 있다. 하지만 현재 성인골수(BM)유래 줄기세포는 그 치료에 한계점 들이 있다. 본 연구에서는 성인골수(BM)유래 줄기세포의 치료 한계점을 극복하기 위하여, 인간 배아줄기세포(hESC)의 분화 및 분리를 통해 일반적인 MSCs의 특성을 나타내는 다능성-줄기세포(M-MSCs)를 생성하는데 성공했다.

염산주입으로 유도된 IC/BPS 동물모델 내에서, BM-MSCs와 비교하여 M-MSCs가 훨씬 더 우수한 효능으로 방광 배뇨기능의 개선과 요로상피세포 결손, 비만 세포 침윤, 조직 섬유증, 세포사멸 및 내장 과민증을 포함한 여러 증상을 완화시켰다. 그리고 공초점 형광 현미경을 이용하여 살아있는 동물에서 6 개월 이상 이식세포의 지속성을 관찰했다. 또한 이식한 줄기세포의 부작용으로 발생 할 수 있는 비정상적인 세포증식이나 종양형성 그리고 이식거부반응과 같은 결과들을 이식 후 12 개월에 걸쳐 관찰하였다. 마지막 조직학적 분석 결과로 이식된 M-MSCs는 여러 유형의 세포로 분화되고 점차적으로 혈관과 유사한 구조로 변하는 것을 확인 했다.

본 연구에서는 IC/BPS의 전임상 모델에서 hESC에서 유래된 M-MSCs의 치료 효능과 더불어, 이식 후 장기적 안정성과 생체 내 분포 및 세포특성에 대한 첫 번째 증거를 제시한다.

## 국문 초록

### 제 2 장.

저활동성 배뇨장애를 재현할 수 있는 만성 허혈성 방광 쥐 모델 개발.

**목적:** 만성 허혈성 방광(CBI)에서의 배뇨장애와 방광기능에 대한 병태 생리학을 연구하고 신뢰성 있는 배뇨근 저활동성(DUA) 쥐 모델을 확립하고자 한다.

**방법:** 16 주령이 된 성체 수컷 쥐의 양측 하복부를 종절개하여 장골동맥을 박리하고, 박리된 장골동맥으로 2 Fr Fogarty 카테터를 사용하여 각각 10 회, 20 회, 30 회로 장골동맥 내강의 혈관내피손상(VED)을 유도 하였다. 장골 동맥 손상 후 8 주동안 2%의 콜레스테롤 식이를 한 장골 동맥손상(AI) 그룹: AI-10; 10 회, AI-20; 20 회, AI-30; 30 회) 세 가지 그룹과 sham 그룹은 2% 콜레스테롤 식이만 받았고, 일반적인 식이요법을 받은 대조군 그룹을 포함하여 총 다섯 그룹으로 나누었다. 8 주 후에 모든 쥐는 마취하지 않은 상태에서 24 시간동안 배뇨활동 분석과 요동학적 검사를 받았다. 그 후 방광 조직은 근육장력 평가, 면역조직화학염색법 그리고 유전자발현 분석을 진행하였다.

**결과:** 24 시간 배뇨활동 분석 결과, AI-30 그룹에서 배뇨간격이 유의하게 증가되었고( $p < 0.001$ ), 배뇨 횟수와 배뇨 양이 유의하게 감소하였다( $p < 0.01$ ,  $p < 0.001$ ). 요동학적 검사로 AI-30 그룹에서는 배뇨 수축 및 배뇨압이 유의하게 낮았다 ( $p < 0.01$ ). 방광근 장력 측정에서, AI-20 과 AI-30 그룹에서 다양한 자극에 대한 수축반응이 유의하게 낮게 나타났다( $p < 0.001$ ). 조직학적 검사에서 AI-20 및 AI-30 그룹의 장골 동맥에서 죽상동맥경화가 관찰 되었으며, 조직염증, 섬유증, 신경세포 감소 및 방광근육조직의 세포사멸이 sham 그룹에 비해 유의하게 증가 되었다. 유전자적 연구에 의하면 만성 허혈성 방광으로 유도된 저활동성 쥐 모델에서 Il-17 과 Hif-1 신호전달 과정을 포함한 Ifn-gamma receptor-1

과 Cxc12 유전자가 상향 조절 되었다

**결론:** 인위적인 약물 없이 쥐 모델에서 혈관내피세포 손상만으로 저활동성 방광을 유도하는데 성공했다. 혈관내피손상으로 인해 점진적으로 산화적 스트레스와 조직염증, 섬유화, 신경세포 감소 및 세포사멸들이 만성 허혈성 방광으로 인한 저활동성 방광 유도를 확인 할 수 있었다.